

Formation of Cool Cores in Galaxy Clusters via Hierarchical Mergers

Patrick M. Motl and Jack O. Burns

Center for Astrophysics and Space Astronomy, University of Colorado, Boulder, CO 80309

Chris Loken

Canadian Institute for Theoretical Astrophysics, McLennan Labs, University of Toronto, 60 St. George, Toronto, Ontario M5S 3H8

Michael L. Norman

Center for Astrophysics and Space Sciences, University of California, San Diego, 9500 Gilman Drive, La Jolla, CA 92093

Greg Bryan

University of Oxford, Astrophysics, Keble Road, Oxford, OX1 3RH

`motl@casa.colorado.edu`

ABSTRACT

We present a new scenario for the formation of cool cores in rich galaxy clusters based on results from recent high spatial dynamic range, adaptive mesh Eulerian hydrodynamic simulations of large-scale structure formation. We find that cores of cool gas, material that would be identified as a classical cooling flow based on its X-ray luminosity excess and temperature profile, are built from the accretion of discrete, stable subclusters. Any “cooling flow” present is overwhelmed by the velocity field within the cluster - the bulk flow of gas through the cluster typically has speeds up to about $2,000 \text{ km s}^{-1}$ and significant rotation is frequently present in the cluster core. The inclusion of consistent initial cosmological conditions for the cluster within its surrounding supercluster environment is crucial when simulating the evolution of cool cores in rich galaxy clusters. This new model for the hierarchical assembly of cool gas naturally explains the high frequency of cool cores in rich galaxy clusters despite the fact that a majority of these clusters show evidence of substructure which is believed to arise from recent merger activity. Furthermore, our simulations generate complex cluster cores in concordance with recent X-ray observations of cool fronts, cool “bullets”, and

filaments in a number of galaxy clusters. Our simulations were computed with a coupled N-body, Eulerian, adaptive mesh refinement, hydrodynamics cosmology code that properly treats the effects of shocks and radiative cooling by the gas. We employ up to seven levels of refinement to attain a peak resolution of $15.6 \text{ h}^{-1} \text{ kpc}$ within a volume $256 \text{ h}^{-1} \text{ Mpc}$ on a side and assume a standard ΛCDM cosmology.

Subject headings: cosmology:theory — galaxies: clusters: general — galaxies: cooling flows — hydrodynamics — methods: numerical

1. Introduction

The potential impact of radiative cooling by the hot intracluster medium (ICM) has been recognized for many years (Cowie & Binney 1977; Fabian & Nulsen 1977). The X-ray emitting gas is trapped in approximate hydrostatic equilibrium in the cluster’s potential well. A “cooling flow” is believed to form as the radiating gas loses pressure support and flows inwards to higher density values thus accelerating the cooling rate. In cooling flow clusters, typically, the gas within approximately 100 kpc of the cluster center has a cooling time less than the age of the cluster. This theoretical scenario is well known (see Fabian 1994 for a review) and, for example, has been examined extensively for its effect on cluster dominant galaxies and to determine the ultimate fate of the cool gas.

Cores of cool gas were found to be quite common in the flux-limited *ROSAT* sample of Peres *et al.* (1998), occurring in 70 to 90 percent of their clusters. Similarly, White *et al.* (1997) found cool cores in $62 \pm 15\%$ of the 207 clusters in their *Einstein* sample. Though these samples are flux limited and will exhibit bias towards intrinsically bright core X-ray clusters, they nonetheless argue for cool cores being a common occurrence in nearby clusters.

Substructure is also a common characteristic in galaxy clusters. For example, in the REFLEX+BCS cluster sample, Schuecker *et al.* (2001) find evidence for substructure in the central 1 Mpc (for $H_0 = 50 \text{ km s}^{-1} \text{ Mpc}^{-1}$) in a majority ($52 \pm 7\%$) of their clusters. The presence of substructure argues for accretion or merger events that occurred sufficiently recently to not be erased by relaxation of the cluster to a spherically symmetric state (Roettiger *et al.* 1996).

The prevalence of both substructure and cool cores presents a puzzle as one might expect mergers to disrupt the cores of cool gas present in one or both clusters before their merger. Sparks (1992), however, argued that it was ultimately accretion events that powered the X-ray excess in cooling flow clusters through conductive heat transport from the hot ICM into

accreted cores of cool gas. While this scenario was later shown by Fabian *et al.* (1994) to be untenable on theoretical grounds, this does not negate the observational arguments that Sparks presented for a correlation between cooling flow and merger signatures in clusters.

Early theoretical work on the merger of galaxy clusters suggested that the X-ray emitting gas will be strongly impacted during the interaction and that cooling flows may be disrupted by mergers though these calculations did not treat the fluid of the intracluster medium (McGlynn & Fabian 1984). While investigating the cluster Abell 2256, Fabian & Daines (1991) concluded that this particular cluster is undergoing a merger currently and suggested that the accreted subcluster may donate pre-cooled gas to seed a future, massive cooling flow. In a series of controlled numerical experiments, Burns *et al.* (1997) and Gómez *et al.* (2002) examined the fate of an idealized, spherical cooling flow cluster in collision with another cluster for a variety of cluster mass ratios (1/4 and 1/16), cooling flow strengths (100 and $400 M_{\odot}\text{yr}^{-1}$) and central densities of the accreted subcluster (1.5×10^{-3} to $1 \times 10^{-4} \text{cm}^{-3}$). They found that the ram pressure of the merging subcluster impacting the cooling flow is the main mechanism for disrupting cooling flows. However, the work of Gómez *et al.* treated the hydrodynamics in two dimensions and considered only collisions at zero impact parameter (head on), thus simulating the most efficient case for disruption. Furthermore, their simulations treated the merging system in isolation from the larger, supercluster environment. Given the simplifications made, these previous results do not reflect the rich complexity of interactions observed in both cosmological simulations and in observations. In more recent work, fully three-dimensional cluster collision calculations have been performed by Ritchie & Thomas (2002) and Ricker & Sarazin (2001). In both investigations the authors find that major mergers disrupt cooling flows.

The formation and evolution of cool cores in a realistic environment can be investigated via numerical simulations that evolve both a collisionless dark matter component and a fluid that approximates baryonic matter from cosmological initial conditions to the present. At a minimum, the numerical algorithm must incorporate energy loss from the fluid by radiation. The majority of numerical simulations that treat radiative cooling by the baryonic component have used the smoothed particle hydrodynamics (SPH) formalism. Early SPH simulations with radiative cooling, starting with the work of Thomas & Couchman (1992) and Katz & White (1993), already found rough agreement with observed systems given the limited resolution possible at the time. However, additional physical processes, supernova feedback in particular, were hinted at being necessary to avoid the “cooling catastrophe”, whereby unrealistically large amounts of fluid would cool. The next generation of SPH calculations (Evrard *et al.* 1994; Frenk *et al.* 1996; Sugimotohara & Ostriker 1998) seemed to confirm the need for additional physics in the simulations and helped to quantify the strong resolution dependence of the over-cooling problem in SPH simulations. In Sugimotohara & Ostriker

(1998), for example, doubling the spatial resolution initiated substantial over-cooling that led to an improbably large X-ray luminosity for their cluster, given the cluster’s average temperature. Star formation was again found to be necessary to prevent the divergence of the central density and X-ray luminosity in the recent, high resolution simulations by Valdarnini (2002). For the SPH simulations of Pearce *et al.* (1999, 2000), realistic clusters were found (with radiative cooling actually lowering the total X-ray luminosity for their clusters) provided that their SPH code was modified as follows. First, cold and hot gas phases were identified and gas in the cold phase was excluded when calculating average density values in nearby regions of hot gas. Second, a minimum mass limit for cooling was enforced and the resolution was set to an optimal value. At higher resolution, however, over-cooling is expected to again contaminate their results. Star formation was incorporated in one of the simulations of Lewis *et al.* (2000) where they examined the properties of a Virgo-like cluster at the present epoch and concluded that cooling with star formation eliminated the problems evidenced in Sugihara & Ostriker (1998). However, in their simulation Lewis *et al.* did find a very large fraction of gas condensing (up to 30%, roughly a factor of three too large compared to observations) despite the energy input from supernova feedback. The phenomenon of over-cooling in SPH simulations has recently been cast in a very interesting light by Tittley *et al.* (2001). Briefly, a numerical “drag” was demonstrated as cold, condensed material traverses a hotter medium, causing spurious over-merging and over-cooling in SPH calculations.

In grid-based (Eulerian) treatments of the hydrodynamics of structure formation, radiative cooling has been included in simulations calculated with a first order accurate scheme (Cen & Ostriker 1992) and recently with a more accurate total variation diminishing (TVD) scheme (Cen & Ostriker 1999). While it is much more straightforward to incorporate additional physics such as star formation and multiple fluid components in grid-based programs, these methods have historically suffered from a lack of spatial resolution when implemented on static, uniform grids. Compared to the resolution of current SPH simulations in dense regions, previous fixed grid Eulerian simulations have about an order of magnitude coarser spatial resolution (roughly 100 kpc in the best cases) if they are to evolve a useful subdomain in the universe. For such simulations, the regions where radiative cooling dominates (roughly 100 kpc) would be unresolved with even a more accurate numerical scheme such as PPM. The partial differential equations of hydrodynamics may, however, be solved on a sequence of nested grids of finer and finer resolution to allow a large range of length scales to be treated. The grid system must be dynamic to follow hierarchical collapse of the fluid during structure formation. We use just such an adaptive mesh refinement (AMR) algorithm to attain the requisite spatial dynamic range to resolve cool cores while retaining the many desirable attributes of Eulerian hydrodynamics techniques.

In the current paper we address the issue of the formation and evolution of cool cores of gas in clusters through direct numerical simulations that proceed from realistic initial conditions. We introduce radiative cooling by the fluid component into our algorithm and evolve clusters from cosmological initial conditions through the non-linear hierarchical assembly phase to the present day. We are thus able to observe merger processes in the simulated clusters where the full complexity of the system - ram pressure stripping, tidal disruption and shock heating - are treated accurately.

In §2 we describe our numerical code noting physical processes that are not included in the current work and their potential importance. In §3 we present our simulation sample, their gross physical properties and compare them to results from other simulations that include the effect of radiative cooling. We then present a brief analysis of a test case where we have performed otherwise identical simulations with and without radiative cooling in §4. In §5 we present an overview of subclusters in our simulations and in §6 we present a history of cluster interactions from a redshift of one to the present. The impact of the cluster environment and subcluster mergers are detailed in §7. We then analyze our simulated data from an observational point of view in §8. Finally we compare our simulation results to recent observational results from *Chandra*, and *XMM* in §9 and summarize our conclusions in §10.

2. Numerical Technique

Our simulation tool is a coupled N-body Eulerian hydrodynamics code (Norman & Bryan 1999; Bryan, Abel & Norman 2001). We use an adaptive particle-mesh, N-body code to evolve dark matter particles. To treat the fluid component, we use the PPM scheme (Colella & Woodward 1984) on a comoving grid. We employ adaptive mesh refinement (AMR) to concentrate our numerical resolution on the collapsed structures that form naturally in cosmological simulations. The dark matter particles exist on the coarsest three grids; each subgrid having twice the spatial resolution in each dimension and eight times the mass resolution relative to its parent grid. At the finest level, each particle has a mass of $9 \times 10^9 h^{-1} M_{\odot}$. We use second order accurate TSC interpolation for the adaptive particle mesh algorithm. Up to seven levels of refinement are utilized for the fluid component for most of the results presented here, yielding a peak resolution of $15.6 h^{-1} \text{ kpc}$ within our simulation box with sides of length $256 h^{-1} \text{ Mpc}$ at the present epoch. We have chosen a standard, flat Λ CDM cosmology with the following parameters: $\Omega_b = 0.026$, $\Omega_m = 0.3$, $\Omega_{\Lambda} = 0.7$, $h = 0.7$, and $\sigma_8 = 0.928$.

The fluid is allowed to radiatively cool in the present simulations. We use a tabulated

cooling curve (Westbury & Henriksen 1992) for a plasma of fixed, 0.3 solar abundance to determine the energy loss to radiation. The cooling curve falls rapidly for temperatures below 10^5 K and is truncated at a minimum temperature of 10^4 K. Heat transport by conduction is neglected in our algorithm and it is expected that even a weak, ordered magnetic field can reduce conduction by two to three orders of magnitude from the Spitzer value (Chandran & Cowley 1998). Indeed, Vikhlinin *et al.* (2001a) find that thermal conduction is suppressed by a factor of 30 to 100 at the interface of the ISM for NGC 4874 in the Coma cluster. While Vikhlinin *et al.* find that conduction is suppressed, the energy transport into NGC 4874 approximately balances the energy lost through radiation and therefore thermal conduction should be included in simulations that treat the detailed state of small scale structures. Furthermore, the theoretical work of Narayan & Medvedev (2001) has shown that if turbulence extends over a sufficiently large range of length scales within the ICM, the effective conductivity coefficient is expected to be about one fifth of the Spitzer value making thermal conductivity significant to the global energy balance of the ICM. The potential importance of including conduction in future work is also bolstered by recent data from Fabian, Voigt & Morris (2002) who report that in a sample of 29 clusters most have an effective conductivity between the Spitzer value and one-tenth the Spitzer value and from Zakamska & Narayan (2003) who show that half of the 10 clusters they studied are consistent with heat transport by conduction balancing radiative cooling.

We also neglect energy input into the fluid from supernovae feedback or discrete sources such as AGN in our current simulations. Lewis *et al.* (2000) have found that supernova feedback and cooling can significantly alter the fluid properties in the centers of clusters though the large scale temperature distribution depends predominantly on shock heating and is relatively insensitive to both supernova feedback and radiative cooling (Davé *et al.* 2001). The expected effect from supernova feedback on our results is two-fold. First, by neglecting additional sources of energy such as supernova feedback our simulations generate cool cores with density profiles that are too steep and thus we will overestimate the resilience of cool cores during mergers. Second, it is precisely the cool material in cores that can collapse to form assemblies of stars, removing that fluid from the flow and yielding a less dense core. Nonetheless, the case of maximal stability for cool cores is of theoretical interest as a limiting case and also as a guide to constrain the largely uncertain parameterization of supernova feedback prescriptions.

As described in Loken *et al.* (2002) we have identified clusters within our $256^3 h^{-3} \text{Mpc}^3$ parent volume and performed AMR simulations of sub-volumes to create a “catalog” of simulated clusters. From this set of adiabatic simulations we present two clusters, chosen because of their interesting merger history, that have been rerun with radiative cooling included. One cluster, hereafter C1, undergoes a major merger between approximately

equal mass components at $z \approx 0.4$ while our second simulation, hereafter referred to as C2, merges with a subcluster of approximately half its mass. In future work, we will present results from an ensemble of radiative cooling clusters to address issues such as the cluster $L_X - T$ relation and the probability of cool core disruption by cluster collisions. For our present purpose we will limit our scope to these two clusters as a guide to interpreting the wealth of recent X-ray observations of galaxy clusters and to emphasize the importance of mergers in assembling cool cores in rich galaxy clusters.

3. Rich Cluster Properties

Projections of the gas density at the present epoch within the refined volumes for our simulated clusters C1 and C2 are shown in Figures 1 and 2 respectively. In both cases we see that the dominant cluster lies at the intersection of a network of filaments that convey material into the clusters. In both figures we have outlined a square region $5 \text{ h}^{-1} \text{ Mpc}$ on a side about the center of mass of each cluster. In subsequent images we will be zooming in on this region to examine the detailed structure present in our clusters. The clusters we present here are the two most massive structures that form in our simulation volume and are exceptional in that respect. They correspond to $R \geq 4$ and $R \geq 3$ clusters for C1 and C2, respectively, given the cluster mass function in Bahcall & Cen (1993). In adiabatic simulations of the clusters, they exhibit a central cooling time shorter than the Hubble time (except for short intervals around major mergers) during the simulations and would therefore be expected to possess cool cores.

In Table 1 we list gross parameters for the clusters C1 and C2 at a redshift of zero. The virial radius, R_{virial} , is calculated for an overdensity $\delta\rho/\rho$ of 200. M_{virial} , M_{dm} , and M_{gas} are the total mass, total mass of dark matter particles, and total fluid mass within the virial radius, respectively. Similarly, L_x is the total X-ray luminosity (line and continuum) within R_{virial} in the 1 to 10 keV band assuming a 0.3 solar metal abundance. The average physical temperature of the ICM within the virial radius is listed as \bar{T} . The velocity dispersion, σ , is the average, three-dimensional velocity dispersion for the dark matter particles within the virial radius and f_{cool} is the ratio of gas mass colder than 15,000 K to the total gas mass within the virial radius.

The properties of our clusters are physically reasonable when compared to actual clusters. In particular, unlike the high resolution simulation of Sugimotohara & Ostriker (1998), we do not find our clusters to be overluminous for their temperature and do not conclude that additional physics is required to offset radiative cooling based on gross cluster properties alone. We note that our simulations have a peak resolution (grid cell size) less than half the

size of the smoothing length for Suginozara and Ostriker’s high resolution (MR) run.

We also find that the fraction of cool gas in our clusters, 8.5% and 11.7%, is in excellent agreement with the observational data for clusters summarized by Balogh *et al.* (2001) and is in reasonable agreement with the numerical results of Pearce *et al.* (2000). We have also rerun our C2 simulation with 6 and 8 levels of refinement (corresponding to peak spatial resolutions of $31.2 \text{ h}^{-1} \text{ kpc}$ and $7.8 \text{ h}^{-1} \text{ kpc}$ respectively). As would be expected, the coarsest simulation produced a cluster with a low fraction of cool gas, 2%, this resolution not being sufficient to accurately treat condensed cores. For the highest resolution simulation, the fraction of cool gas within the virial radius is 9.9% - nearly identical to the result listed in Table 1 for our 7 level calculation. Other cluster properties are similar between the 7 and 8 level simulations. We would like to emphasize that we do not see large f_{cool} values for rich clusters as has been reported in recent smoothed-particle hydrodynamics (SPH) simulations (Pearce *et al.* 2000; Lewis *et al.* 2000; Suginozara & Ostriker 1998) nor do we find that the fraction grows as our resolution improves beyond that used for the results presented here.

4. Comparison to Adiabatic Simulations

We have, as a test, performed simulations of the same refined volumes in the adiabatic limit and with radiative cooling. In Figure 3 we show projections of the X-ray luminosity (top row) and emission-weighted temperature (bottom row) for the adiabatic and radiative cooling realizations of C1 at the present epoch. The image scales are indicated by the color bars and the surface brightness has been normalized to its maximum value. The most noticeable distinction is that when radiative cooling is included, subclusters form dense cores of cool gas (bright and dark blobs in the X-ray and temperature images, respectively) as expected and seen in previous simulations (c.f. Katz & White 1993). In particular note the tight, high density core of cool gas at the center of the primary cluster (the cluster center of mass is indicated by the tick marks for reference). As infalling cores interact with the primary cluster, they produce complex structures such as the bow shock and “comet tail” associated with the subcluster to the bottom of the cluster center and the extended, irregular distribution of cool gas (“cool front”) to the bottom right of the cluster center. Without the density enhancement generated by cooling, the collisions of clusters in the adiabatic simulations lack this rich structure.

The larger scale structure of the adiabatic and cooling clusters are generally similar, however, as they are dictated by the overall cluster properties rather than perturbative interactions. For example, the ridge of shocked, hot gas at the bottom of the clusters is in nearly the same location in both the radiative cooling and adiabatic simulations and has

comparable temperatures in both cases.

As another example, Figure 4 shows images for the C2 simulation at a redshift of 0.25. Again, a core of dense cool gas is readily apparent in the radiative cooling results though the core is more regular in this instance. This snapshot also demonstrates cluster interactions; a subcluster can be seen below the cluster center of mass with a leading shock front and a trailing stream of stripped, cooler gas. While the filamentary network is bringing material into the cluster in the same manner in both the radiative cooling and adiabatic simulations, the infalling subclusters are much more condensed in the radiative cooling simulation and are hence more readily apparent. The more strongly peaked density profile also serves to shield the infalling cluster from disruption. This core of cool gas has survived a cluster crossing with only some ram pressure stripping and tidal stripping in evidence. In the adiabatic case, this infalling cluster was absorbed into the primary ICM with only a relatively small elongation of the central surface brightness distribution and small shock front at the bottom of the cluster to betray its presence.

In Figure 5 we show profiles of the X-ray surface brightness and the projected, X-ray emission-weighted gas temperature corresponding to the snapshots shown in Figures 3 and 4. The results from the adiabatic simulations are drawn as dashed curves while the radiative cooling profiles are solid lines. Both C1 and C2 show an excess X-ray luminosity and falling temperature within about $100 \text{ h}^{-1} \text{ kpc}$ of the cluster center, as would be expected for a cool core. Outside of the core there is little difference between the adiabatic and radiative cooling simulations in spite of the rich structure of cool gas clumps in the images. Also note that the gas in the core is not very cool, remaining above a million Kelvin for both simulations. As noted in §2 our cooling function continues down to approximately 10^4 K meaning that the fluid can lose energy by radiation until this floor value is reached (neglecting temperature changes due to mechanical work on the fluid). The high temperatures of the “cool” gas in our cooling clusters is due to two effects. First, we have shown the profiles derived from a projection of the temperature field onto the plane of the sky. The cool core is seen along with the hotter material lying along the line of sight. Second, as will be discussed in more detail later, the physical temperature of the core reaches values above 10^6 K . There are only two means of heating possible given the assumptions we have made for these simulations: shock heating and adiabatic compression. We find this to argue for the importance of accurately treating shocks in the ICM.

5. Subcluster Properties

The vast majority of cluster interactions in our simulations can be described as accretion of smaller subclusters by the dominant cluster. In this section we detail the properties of these subclusters. In Table 2 we list gross properties for a sample of outlying subclusters that reside between 2 and 5 h^{-1} Mpc of C1’s center of mass at a redshift of zero. Of these 13 subclusters, ten are falling in for the first time. Two of the subclusters (the first and third entry in Table 2) are climbing out of the cluster potential well at the current epoch and one subcluster (the fifth entry) has orbited about the main cluster for the past six billion years at a typical separation between 2 and 3 Mpc.

In Table 2, we list the distance from the C1 center of mass which helps gauge how well the subclusters may be treated as isolated systems. We also list the virial radius, virial mass, the total dark matter and fluid mass and X-ray luminosity within R_{virial} . We tabulate the average physical temperature of the gas within the virial radius (\bar{T}) and within a core of 50 kpc (T_{core}), the average, three-dimensional velocity dispersion of dark matter within the virial radius, the fraction of gas that is cooler than 15,000 K within the subcluster, the average cooling time within the core and the virial ratio for the subcluster. The virial ratio is computed as $\sigma^2 M_{\text{virial}} / |W|$ where σ is the previously described velocity dispersion and W is the gravitational potential energy calculated from spherically averaged profiles of the dark matter distribution from

$$W = -4\pi G \int_0^{R_{\text{virial}}} \rho(r) M(r) r dr. \quad (1)$$

The virial ratio is expected to be approximately unity for isolated structures in virial equilibrium. The two subclusters with a measured virial ratio greater than 2 have already interacted with the main cluster before this time and in particular, the fifth subcluster (with a virial ratio of 4.1) has orbited within the clusters virial radius for a significant fraction of the simulation. The pristine, infalling subclusters are all relatively well described as gravitationally bound systems in virial equilibrium.

Overall, the subclusters have properties similar to galaxy groups (in terms of extent, mass, average temperature and luminosity). Their baryons are locked in cool, condensed gas; all subclusters have low core temperatures and high fractions of cool material. Furthermore, the cooling time is much shorter than the Hubble time for all subclusters in Table 2. In our simulations we have only included the effect of radiative cooling without any heat sources or transport mechanisms beyond the adiabatic physics level. For this set of assumptions, an isolated subcluster has no recourse but to cool a large fraction of its baryons.

Given the large fraction of cool material, star formation feedback will obviously impact

the detailed structure of these subsystems. They will, however, likely remain as gravitationally bound structures and act as sources of condensed gas for the rich clusters that form from them. As mentioned previously, we are focusing our attention on the properties of rich clusters and considering only the limiting case where radiative cooling is as efficient as possible.

6. Merger Histories

In this section we present a detailed discussion of the history of our simulated clusters. In Figure 7 we show projected, normalized X-ray surface brightness and X-ray emission-weighted temperature maps for C1 from a redshift of one to the present day in approximately 500 million year intervals. The images have all been scaled to the same range of values so that a given color corresponds to the same value (within the discreteness of the color map) throughout the sequence of images. We note that the X-ray images have been prepared to emphasize the rich substructure by firstly showing all pixels with a surface brightness 1% or greater than the peak as white. Secondly, the dynamic range extends far beyond that possible with current observations (please note the color bars in Figure 7). On this scale, there is a very rich array of subclusters and substructure visible. In Figure 6 we show the X-ray surface brightness for C1 at the present epoch with three example image scales. For a more realistic dynamic range of 10^3 there is only one structure feature visible within 1.5 Mpc of the cluster center of mass. For observations with a dynamic range of 10^4 there are two subclusters visible within an Abell radius while the remainder of projected subclusters and substructure seen in Figure 7 are fainter still.

At $z = 1$ the primary has a regular core of cool gas though it is interacting with a set of irregular subclusters to the lower left and a comparable mass cluster is assembling to the far right (in projection). Through a redshift of 0.75 the primary core is bar shaped and there are several filaments of cool, dense gas running through the cluster.

Interactions continue through a redshift of 0.5 when the central cool core is noticeably reduced in extent in the temperature map. At this epoch the cluster to the right is still taking shape and is moving closer to the primary through $z = 0.43$ and finally collides nearly head on with the primary at a redshift of 0.37. There is a collar of shock-heated gas surrounding the core at this epoch which expands outwards. The impactor reaches its turning point after passing through the cluster at approximately $z = 0.3$. There is a strong shock front at the head of the impactor and a trail of cooler gas leading back from the shock front to the cluster center. Surprisingly, a core of cool gas is still visible at the cluster center of mass.

By $z = 0.25$ the impactor has fallen back towards the center and there is a binary cool core system that persists through $z = 0.21$. At $z = 0.25$ the shock fronts continue to expand away from the cluster center. The binary cores have merged by $z = 0.16$ and the core is rather small in extent. From $z = 0.12$ to 0.08 a smaller subcluster passes through from left to right across the cluster and from $z = 0.08$ to the present a set of subclusters fall through the cluster from the upper left to the bottom right, one of which produces a significant bow shock ahead of it and is finally disrupted at $z = 0.0$ into an irregular patch of cool gas (also see Figure 3 for an enlarged view of this cluster at $z = 0$).

Similar images for C2 are shown in Figure 8. The C2 sequence begins as the primary cluster has merged with a subcluster of about half its mass. The cores of the two systems nearly overlap one another at the cluster center. There are, in addition, several smaller scale interactions lasting to $z = 0.65$. From $z = 0.65$ through $z = 0.43$ the primary cluster is left largely unperturbed. Nonetheless, the central cool core is almost totally absent at $z = 0.5$. From $z = 0.37$ through to $z = 0.12$ a cluster with about 5% of the mass of the primary falls from top to bottom through the cluster. It passes through the cluster center between redshifts of 0.31 and 0.25 and excites a spherical shock wave that expands through the cluster from redshifts of 0.25 to 0.16 . The infalling cluster is disrupted by the encounter, ultimately becoming the “Y” shaped structure below the primary cluster in the snapshots at 0.16 and 0.12 . Excepting a few minor, off axis, interactions the C2 system is left largely undisturbed from $z = 0.25$ to the present. It is interesting to note that the central cool core does not regain a spherical shape in this intervening time, remaining instead bar-like in this projection.

As a means of gauging the disruption of the cool cores we plot the X-ray surface brightness and spherically averaged temperature profiles for clusters C1 and C2 at a variety of redshifts in Figures 9 and 10 respectively. The temperature profiles for both clusters are very complex, though in all cases there is cool gas in a core of some form. The temperature curve for C1 at $z = 0.25$ has an odd shape because there are two cool cores in a binary at this epoch and the profiles are taken about the center of mass of the cluster as a whole which lies between the two cores. The smoothing over the binary core system is also responsible for the isothermal profile shape for the X-ray surface brightness of C1 at $z = 0.25$. At $z = 0.31$, however, the X-ray surface brightness signature of a cool core is washed out by the recent passing of the companion cluster through the primary. At redshifts of $z = 1$ and 0.84 , C1 again does not exhibit an X-ray excess. For C2 the surface brightness profiles are much more straightforward; for all redshifts from 0.43 to 1 (with the exception of 0.57) there is no evidence for an X-ray excess. From 0.37 up to the present, C2 does not suffer any major interactions and shows a remarkably static luminosity excess from its cool core.

From an observational point of view, one may see clear evidence for a cool core at only certain points in the cluster’s history. If there has been a major merger event or frequent, though less extreme interactions, the cool core signature may disappear in the X-ray surface brightness. However, cool gas remains in these two systems at all times, despite the vigorous merger activity.

7. The Dynamical Cluster Environment

In this section we further explore the complex dynamical environment that acts on the cool core clusters. We note in particular that our simulation results are inconsistent with expectations arising from the simple cooling flow model for an isolated cluster. The dynamical cluster environment is seen very clearly from the velocity field which we plot for 4 epochs for cluster C1 in Figure 11. These are representative examples of the flow field; similar features are seen for both clusters and for other slices through the clusters. We plot the velocity in the x-y plane for a $1 \text{ h}^{-1} \text{ Mpc}$ region centered on the cluster center of mass. At a redshift of 0.25, two cores are about to collide with one another and a similar collision is seen at a redshift of 0 where a subcluster has passed through the core. In all plots, the velocity field is irregular with material streaming through the cluster core. Recall that the clusters lie at the intersection of filaments (see for example Figures 1 and 2) that flow into the clusters. The asymmetric streams result in a complex flow field that dominates over the orderly, spherically symmetric radial flow of material arising from a “cooling flow”. In addition to the features exemplified in Figure 11, we also see circulation within the cluster center. The rotation arises from the residual angular momentum of merging structures colliding at non-zero impact parameter.

The response of the cool core is characterized in Figure 12 where we plot the following quantities versus the lookback time (and redshift) for the C1 and C2 clusters: (1) the amount of cool gas (gas with temperature less than 15,000 K) within $100 \text{ h}^{-1} \text{ kpc}$ of the cluster center of mass, (2) the cooling radius, that is the radius where the cooling time equals the Hubble time at that particular redshift, (3) the characteristic core temperatures of the gas which we take to be the average temperature within 50 kpc of the cluster center of mass, and (4) the fraction of gas cooler than 15,000 K within the virial radius. The characteristic temperature is calculated from both a spherical average of the gas temperature (solid curve) and from a circular region of 50 kpc radius from the projected, emission-weighted temperature (dashed curve). Recall from the discussion in §5 that C1 experiences a major merger that lasts from $z = 0.37$ to $z = 0.21$ and several minor interactions. C2 experiences a major interaction at $z = 1$.

The mass of cool gas grows for both clusters, though it often increases by discrete units causing peaks in the plots of cool mass. For C1 at $z = 0.25$, the sharp drop in cool gas mass is due to a binary core system orbiting the cluster center of mass beyond our chosen aperture of $100 \text{ h}^{-1} \text{ kpc}$ for this measurement. The mergers are complicated phenomena, infalling cores both donate cool material to the core and shock heat the ICM which mixes hot fluid into the core material.

The cooling radius shown in the second row of plots in Figure 12 also changes abruptly. As dense, condensed material accumulates in the core the cooling time drops causing the cooling radius to grow. During the quiescent period for C2 (from Figure 10, the epochs where there is a static luminosity excess, $z = 0.5$ to 0) the cooling radius grows slowly with time. The characteristic core temperature is shown in the third row of plots in Figure 12. The projected temperature is at nearly all times systematically higher than the physical core temperature and responds less strongly to merger events. The characteristic physical temperature of the core exhibits abrupt changes as shocks arising from the cluster collisions heat fluid in and around the core. We also note that the characteristic projected temperature for the cores of C1 and C2 agree with recent observations of cool core clusters where minimum temperatures have been consistently found to be approximately one keV for a variety of clusters (Fabian 2002). For a global view of the evolution of clusters C1 and C2, we also show the fraction of gas cooler than 15,000 K within the virial radius (f_{cool} from Tables 1 and 2). Cool gas is present in both clusters throughout their evolution despite collisions. As subclusters fall in (objects with a majority of their baryons in a cool phase as shown in Table 2) most of their baryons are heated by shocks and compression so that as the cluster grows in mass, the cool fraction generally declines with time. However, as noted previously, some cool gas survives these interactions and merges in the cluster core as well. As an example of the interaction process, a typical infalling cluster at a redshift of 0.5 will lose $\approx 90\%$ of its total gas and typically $\approx 70\%$ of its core mass (the cool gas) has been heated and lost to the cluster during a crossing (see Figures 7 and 8). These results, of course, can vary widely depending on the trajectory of the infalling subcluster and the state of both systems.

The main point of this examination of the cores is that the mass of cool gas in the central core grows predominantly from the accretion of discrete subclusters that contain pre-cooled gas and not from steady state cooling. We do not find any evidence for a “cooling flow” in our simulations, in accord with the recent simulations of Lewis *et al.* (2000) who find the flux of mass in adiabatic and radiative cooling simulations agree with one another in to a distance of 40 kpc from the cluster center. For our C1 and C2 clusters, the random flow of fluid in the cluster center (characterized by the average velocity dispersion for the fluid within the cooling radius) exceeds the mean radial velocity by a factor of approximately 25 (see also Figure 11). This is clearly inconsistent with the classical cooling flow scenario.

On average, C1 and C2 gain cool material at a rate of about $600 M_{\odot}\text{yr}^{-1}$ from a redshift of 2 to the present but this is predominantly due to merger events. In Figures 13 and 14 we show the flux of cool material through spheres of radius 0.1, 0.5 and 1.0 Mpc centered on the cluster center of mass for C1 and C2, respectively. If, for example, a blob of material crossed through the cluster without interacting at a constant velocity of $1,000 \text{ km s}^{-1}$ it would appear as a negative and then positive peak in these plots, separated in time by approximately 2 billion years. One might also expect that as cool cores rain in on the cluster they would appear in these plots as a set of three peaks as they successively cross from 1 to 0.5 to 0.1 Mpc. Figures 13 and 14 show that the situation is more complicated than this expectation. In Figure 13 for example, there is little flux of cool material through the surface at a 500 kpc while we can clearly see cores crossing at the other two radii. The situation for C2 is largely similar though we can see that this cluster has a more gentle evolution (note the different scales for Figures 13 and 14). From a redshift of approximately 0.6 to the present, C2 is left largely undisturbed and there is an indication that cool material is settling on the core given the small, approximately constant flux of material through the inner surface for the past 2 billion years.

As has been demonstrated several times, the evolution of these simulated cool core clusters is complex. Even at the present epoch, the clusters do not represent relaxed, steady state structures as can be seen from Figures 7 and 8 for instance. The full complexity of the merger history of the clusters is intrinsically tied to the formation of cool cores in our simulations. This stands in stark contrast to the classical cooling flow scenario where a spherically symmetric distribution of gas cools in isolation and, in particular, is not perturbed by accretion or major merger events with other cool cores.

8. Observational Analysis

If we analyze our simulated clusters from the point of view of an observer, they would be identified as a “cooling flow” cluster if they exhibit an X-ray excess over an isothermal sphere model and/or have lower temperatures at the center. No actual flow has ever been detected, nor could be detected with current X-ray spectrometers.

In the simplest application, one ascribes all the excess luminosity to a cooling flow according to the prescription (Fabian 1994)

$$L_{\text{cool}} = \frac{5}{2} \frac{\dot{M}}{\mu m} k_B T. \quad (2)$$

We have fit isothermal sphere models to our surface brightness profiles to determine the luminosity excess (surface brightness and best fit isothermal models are shown at selected

epochs for C2 in Figure 15). Applying equation (2) to C2 (given the known temperature distribution within the cluster) results in the mass deposition rates shown in Figure 15. This method gives reasonable mass deposition rates (in comparison to observations) though as has been previously demonstrated, there is not a real flow present in our simulations.

The hierarchical merger scenario for cool cores provides a physical basis for the results of Loken *et al.* (1999). In their analysis they consider a nearly complete, volume-limited sample of nearby ($z < 0.1$) Abell clusters. To a high degree of significance, Loken *et al.* find that massive cooling flow clusters ($\dot{M} > 100M_{\odot} yr^{-1}$) have closer nearest neighbors and reside in more crowded environments than clusters without cooling flows. If cool cores in rich clusters are built primarily through merger events, massive cool cores will have to reside in dense environments for there to be a sufficient merger rate. As seen in our simulations, mergers can disrupt the X-ray signature of a cool core, though inevitably the core is renewed. Clusters with significant substructure may or may not show evidence for a cool core, depending on the details of the particular merger history but cool core clusters will be predisposed to reside in overly dense regions of the universe.

9. Comparison to Recent Cluster X-ray Observations

Recent, high resolution observations with *Chandra* and *XMM* have revealed new levels of detail in galaxy clusters. What was seen with previous instruments to be relaxed, smooth clusters now show evidence for a dynamic nature. From Figures 7 and 8 we see that our simulations also demonstrate a rich array of cluster substructure and remnant signatures of interactions in the projected temperature maps.

Many clusters have been found to contain “cool fronts” - clouds of cool gas embedded in the hot ICM. Examples include Abell 2142 (Markevitch *et al.* 2000), Abell 3667 (Vikhlinin *et al.* 2001b), RXJ1720+2638 (Mazzotta *et al.* 2001), Abell 85 (Kempner *et al.* 2002), the Centaurus cluster (Sanders & Fabian 2002), MS 1455.0+2232 (Mazzotta *et al.* 2002), Abell 754, and Abell 2163 (Markevitch *et al.* 2001) which all show evidence of a contact discontinuity between an irregular distribution of cool gas and the ICM. An example of a cool front in a cluster is shown in the upper left panel of Figure 16 where we reproduce data for Abell 2142 (Markevitch *et al.* 2000). The temperature maps from figures 7 and 8 provide evidence for a natural explanation for the clouds observed in cool front clusters in terms of hydrodynamical effects from cluster collisions.

A striking example of the complex structure of cool gas was recently discovered by Fabian *et al.* (2001) in Abell 1795. We show the adaptively smoothed *Chandra* image of

the core of Abell 1795, a well known cool core cluster, in the upper right panel of Figure 16. The image is approximately 80 kpc across. From our simulations, we find that similar filamentary structures can be formed from the relative motion of a condensed core of cool material through a hot medium.

In our hierarchical merger model, cluster mergers bring cool material into the accreting cluster. An infalling core was recently reported from *Chandra* observations of 1E0657-56 (Markevitch *et al.* 2002) which is shown in the bottom left panel of Figure 16. They term the infalling system a “bullet subcluster”, the bullet being a core of cool gas (between two and three times cooler than the cluster average) traversing the primary cluster with a prominent bow shock plowing through the cluster medium reminiscent of interactions seen frequently in our simulations.

At higher redshifts, cluster interactions become more frequent. Our cluster C2 is relatively quiescent from a redshift of a half to the present - the bulk of its accretion occurring further in the past. A relatively distant cluster is shown in the bottom right panel of Figure 16. At a redshift of $z = 0.407$, CL 0939+4713 (which was observed with *XMM* by De Filippis *et. al* 2001) shows significant substructure. In the image there are several peaks in the central X-ray distribution (though the peaks labeled P1 and P2 represent a foreground source and a background quasar and do not indicate substructure). Their 1 arcminute bar corresponds to approximately 300 kpc for our chosen cosmological parameters.

10. Conclusions

From the simulation results presented here, we see that the formation and evolution of cool cores in rich galaxy clusters is a highly dynamic process, even to the present epoch. The cluster appearance is shaped by hydrodynamical interactions between condensed cores of cool gas and the hot intracluster medium. Because of these complex interactions, the central cool cores depart significantly from spherical symmetry and do not correspond to the picture evoked by the steady state cooling flow model.

We find that accreted cool cores can survive a transit through the cluster and, more importantly, can donate pre-cooled gas to the accretor. Thus, as rich clusters are assembled through the hierarchical merger scenario of the cold dark matter model, cool cores are built simultaneously from the baryonic fluid component. We note that our simulations have only treated the case of maximal cooling in the sense that heat transport by conduction and energy input are neglected. Our accreted subclusters thus have a steeper density profile than is expected for real clusters and this in turn overestimates the stability of merger subunits in

our simulations. In future work we will investigate the impact of star formation feedback and thermal conduction on our current simulation results. We have also only presented results from the most massive clusters in our simulation archive. In future work we will present a detailed analysis of cluster-cluster and cluster-subcluster interactions seen in our complete sample of simulated galaxy clusters evolved in the limit of radiative cooling only.

In both radiative cooling clusters presented in the current work, we see no evidence for a cooling flow despite the fact that we have sufficient numerical resolution to marginally resolve a vigorous cooling flow if one were present. We instead find that cooling cores gain cool gas through discrete accretion events and that the cluster’s intrinsic velocity field would overwhelm the expected field implied by a cooling flow model. We emphasize that the cool cores in our simulations are dynamic systems, tightly coupled to events in the surrounding intracluster medium.

The model of hierarchical assembly of cool cores naturally accounts for the rich array of structure reported in recent X-ray observations in terms of merger processes. Likewise, the model accounts for the prevalence of both cluster substructure (evidence of merger activity) and cool cores in clusters of galaxies. It also provides a physical basis for the result that massive cool cores are found preferentially in dense supercluster environments (Loken *et al.* 1999).

11. Acknowledgments

PMM wishes to thank Romeel Davé for helpful comments on the manuscript. The simulations presented in this paper were carried out on the Origin2000 system at the National Center for Supercomputing Applications at the University of Illinois, Urbana-Champaign with computer allocation grant AST010014N.

REFERENCES

- Bahcall, N. A., & Cen, R. 1993, ApJ, 407, L49
- Balogh, M. L., Pearce, F. R., Bower, R. G., & Kay, S. T. 2001, MNRAS, 326, 1228
- Bryan, G. L., Abel, T., & Norman, M. L. 2001 in Proceedings of Supercomputing 2001
<http://www.sc2001.org/>
- Burns, J. O., Loken, C., Gómez, P., Rizza, E., Bliton, M., & Ledlow, M. 1997 in Galactic and Cluster Cooling Flows, ed. N. Soker, (San Francisco: ASP), 115, p21

- Chandran, B. D. G., & Cowley, S. C. 1998, *Phys. Rev. Lett.*, 80, 3077
- Cen, R., & Ostriker, J. P. 1992, *ApJ*, 393, 22
- Cen, R., & Ostriker, J. P. 1999, *ApJ*, 519, L109
- Colella, P., & Woodward, P. R. 1984, *J. Comput. Phys.*, 54, 174
- Cowie, L. L., & Binney, J. 1977, *ApJ*, 215, 723
- Davé R., Cen, R., Ostriker, J. P., Bryan, G. L., Hernquist, L., Katz, N., Weinberg, D. H., Norman, M. L. & O’Shea, B. 2001, *ApJ*, 552, 473
- De Filippis, E., Schindler, S., & Castillo-Morales, A. 2001 in *New Visions of the X-Ray Universe in the XMM-Newton and Chandra Era*, eds. F. Jansen *et al.* ESA WPP Conference Series 488 (astro-ph/0201349)
- Evrard, A. E., Summers, F. J., & Davis, M. 1994, *ApJ*, 422, 11
- Fabian, A. C., & Nulsen, P. E. J. 1977, *MNRAS*, 180, 479
- Fabian, A. C., & Daines, S. J. 1991, *MNRAS*, 252, 17
- Fabian, A. C. 1994, *ARA&A*, 32, 277
- Fabian, A. C., Canizares, C. R., & Böhringer H. 1994, *ApJ*, 425, 40
- Fabian, A. C., Sanders, J. S., Ettori, S., Taylor, G. B., Allen, S.W., Crawford, C. S., Iwasawa, K., & Johnstone, R. M. 2001, *MNRAS*, 321, L33.
- Fabian, A. C. 2002 in *Lighthouses of the Universe*, eds. Gilfanov, M., Sunyaev, R., & E. Churazov (Heidelberg: Springer-Verlag) (astro-ph/0201386)
- Fabian, A. C., Voigt, L. M., & Morris, R. G. 2002, *MNRAS*, 335, L71
- Frenk, C. S., Evrard, A. E., White, S. D. M., Summers, F. J. 1996, *ApJ*, 472, 460
- Gómez, P. L., Loken, C., Roettiger, K., & Burns, J. O. 2002, *ApJ*, 569, 122
- Katz, N., & White, S. D. M. 1993, *ApJ*, 412, 455
- Kempner, J., Sarazin, C. L., & Ricker, P. R. 2002, *ApJ*, in press
- Lewis, G. F., Babul, A., Katz, N., Quinn, T., Hernquist, L., & Weinberg, D. H. 2000, *ApJ*, 536, 623

- Loken, C., Melott, A. L., & Miller, C. J. 1999, *ApJ*, 520, L5
- Loken, C., Norman, M. L., Nelson, E., Burns, J. O., Bryan, G. L., & Motl, P. M. 2002, *ApJ*, 579, 571
- Markevitch, M. *et al.* 2000, *ApJ*, 541, 542
- Markevitch, M., Vikhlinin, A., Mazzotta, P., & Van Speybroeck L. 2001 in *X-ray Astronomy 2000*, eds. R. Giacconi, L. Stella, & S. Serio (San Francisco: ASP)
- Markevitch, M., Gonzalez, A. H., David, L., Vikhlinin, A., Murray, S., Forman, W. R., Jones, C., & Tucker, W. 2002, *ApJ*, 567, L27
- Mazzotta, P., Markevitch, M., Vikhlinin, A., Forman, W. R., David, L. P., & Van Speybroeck, L. 2001, *ApJ*, 555, 205
- Mazzotta, P., Markevitch, M., Forman, W. R., Jones, C., Vikhlinin, A., & Van Speybroeck, L. 2002, *ApJin press*
- McGlynn, T. A., & Fabian, A. C. 1984, *MNRAS*, 208, 709
- Narayan, R., & Medvedev, M. V. 2001, *ApJ*, 562, L132
- Norman, M. L., & Bryan, G. L. 1999 in *ASSL Vol. 240: Numerical Astrophysics*, eds. S. M. Miyama, K. Tomisaka, & T. Hanawa, (Boston: Kluwer), 19
- Pearce, F. R., Jenkins, A., Frenk, C. S., Colberg, J. M., White, S. D. M., Thomas, P. A., Couchman, H. M. P., Peacock, J. A., & Efsathiou, G. 1999, *ApJ*, 521, L99
- Pearce, F. R., Thomas, P. A., Couchman, H. M. P., & Edge, A. C. 2000, *MNRAS*, 317, 1029
- Peres, C. B., Fabian, A. C., Edge, A. C., Allen, S. W., Johnstone, R. M., & White, D. A. 1998, *MNRAS*, 298, 416
- Ricker, P. M., & Sarazin, C. L. 2001, *ApJ*, 561, 621
- Ritchie, B. W., & Thomas, P. A. 2002, *MNRAS*, 329, 675
- Roettiger, K., Burns, J. O., & Loken, C. 1996, *ApJ*, 473, 651
- Sanders, J. S., & Fabian, A. C. 2002, *MNRAS*, 331, 273
- Schuecker, P., Böhringer, H., Reiprich, T. H., & Feretti, L. 2001, *A&A*, 378, 408
- Sparks, W. B. 1992, *ApJ*, 399, 66

- Suginohara, T., & Ostriker, J. P. 1998, *ApJ*, 507, 16
- Thomas, P. A., & Couchman, H. M. P. 1992, *MNRAS*, 257, 11
- Tittley, E. R., Pearce, F. R., & Couchman, H. M. P. 2001, *ApJ*, 561, 69
- Valdarnini, R. 2002, *ApJ*, 567, 741
- Vikhlinin, A., Markevitch, M., Forman, W. R., & Jones, C. 2001a, *ApJ*, L87
- Vikhlinin, A., Markevitch, M., & Murray, S. S. 2001b, *ApJ*, 551, 160
- Westbury, C. F., & Henriksen, R. N. 1992 *ApJ*, 338, 64
- White, D. A., Jones, C., & Forman, W. 1997 *MNRAS*, 292, 419
- Zakamska, N. L., & Narayan, R. 2003, *ApJ*, 582, 162

Table 1. Cluster Properties

	C1	C2
R_{virial}	2.7 Mpc	2.4 Mpc
M_{virial}	$2.1 \times 10^{15} M_{\odot}$	$1.5 \times 10^{15} M_{\odot}$
M_{dm}	$2.0 \times 10^{15} M_{\odot}$	$1.4 \times 10^{15} M_{\odot}$
M_{gas}	$1.2 \times 10^{14} M_{\odot}$	$9.0 \times 10^{13} M_{\odot}$
L_x	$3.0 \times 10^{45} \text{ erg s}^{-1}$	$5.0 \times 10^{44} \text{ erg s}^{-1}$
\bar{T}	$8.0 \times 10^7 \text{ K (6.9 keV)}$	$6.3 \times 10^7 \text{ K (5.4 keV)}$
σ	$2,300 \text{ km s}^{-1}$	$1,900 \text{ km s}^{-1}$
f_{cool}	0.085	0.117

Table 2. Subcluster Properties

d (Mpc)	R_{virial} (Mpc)	M_{virial} (M_{\odot})	M_{dm} (M_{\odot})	M_{gas} (M_{\odot})	L_X (erg s^{-1})	\bar{T} (K)	T_{core} (K)	σ (km s^{-1})	f_{cool}	t_{cool} (yr)	VirialRatio
2.2	0.90	8.2×10^{13}	7.9×10^{13}	3.1×10^{12}	3.8×10^{41}	5.0×10^7	2.3×10^5	820	0.45	1.4×10^8	1.9 [†]
3.0	0.49	1.4×10^{13}	1.3×10^{13}	8.1×10^{11}	1.6×10^{40}	9.4×10^6	8.2×10^3	470	0.61	2.1×10^8	1.8
3.4	0.41	7.8×10^{12}	7.2×10^{12}	5.4×10^{11}	2.5×10^{40}	9.4×10^6	1.0×10^5	480	0.81	7.7×10^8	2.2 [†]
4.6	0.40	7.4×10^{12}	7.0×10^{12}	4.3×10^{11}	1.3×10^{39}	2.3×10^6	8.5×10^3	340	0.64	3.6×10^8	1.4
2.7	0.36	5.4×10^{12}	5.4×10^{12}	7.5×10^{10}	4.8×10^{38}	1.8×10^7	8.4×10^3	500	0.46	1.1×10^9	4.1 [†]
3.9	0.36	5.2×10^{12}	4.9×10^{12}	3.4×10^{11}	1.1×10^{39}	6.7×10^6	7.9×10^3	360	0.45	3.6×10^8	1.7
4.8	0.32	3.8×10^{12}	3.7×10^{12}	8.3×10^{10}	3.3×10^{38}	5.5×10^6	8.9×10^3	300	0.47	1.0×10^9	1.4
2.5	0.32	3.7×10^{12}	3.5×10^{12}	1.4×10^{11}	3.9×10^{39}	2.3×10^7	2.1×10^4	310	0.39	8.7×10^8	1.6
4.9	0.31	3.3×10^{12}	3.1×10^{12}	1.6×10^{11}	2.3×10^{37}	2.6×10^6	9.4×10^3	260	0.86	3.6×10^8	1.2
3.9	0.28	2.5×10^{12}	2.4×10^{12}	1.0×10^{11}	4.4×10^{36}	2.6×10^6	9.4×10^3	260	0.86	3.6×10^8	1.2
4.1	0.27	2.1×10^{12}	2.0×10^{12}	1.3×10^{11}	1.8×10^{37}	2.7×10^6	7.8×10^3	200	0.81	5.5×10^8	0.9
4.9	0.26	1.9×10^{12}	1.8×10^{12}	1.7×10^{11}	2.2×10^{37}	1.4×10^6	8.6×10^3	200	0.82	4.3×10^8	0.9
4.7	0.22	1.2×10^{12}	1.1×10^{12}	7.0×10^{10}	4.5×10^{36}	7.7×10^5	8.7×10^3	130	0.76	7.7×10^8	0.8

Note. — † Subcluster passed within 2 Mpc of the main cluster

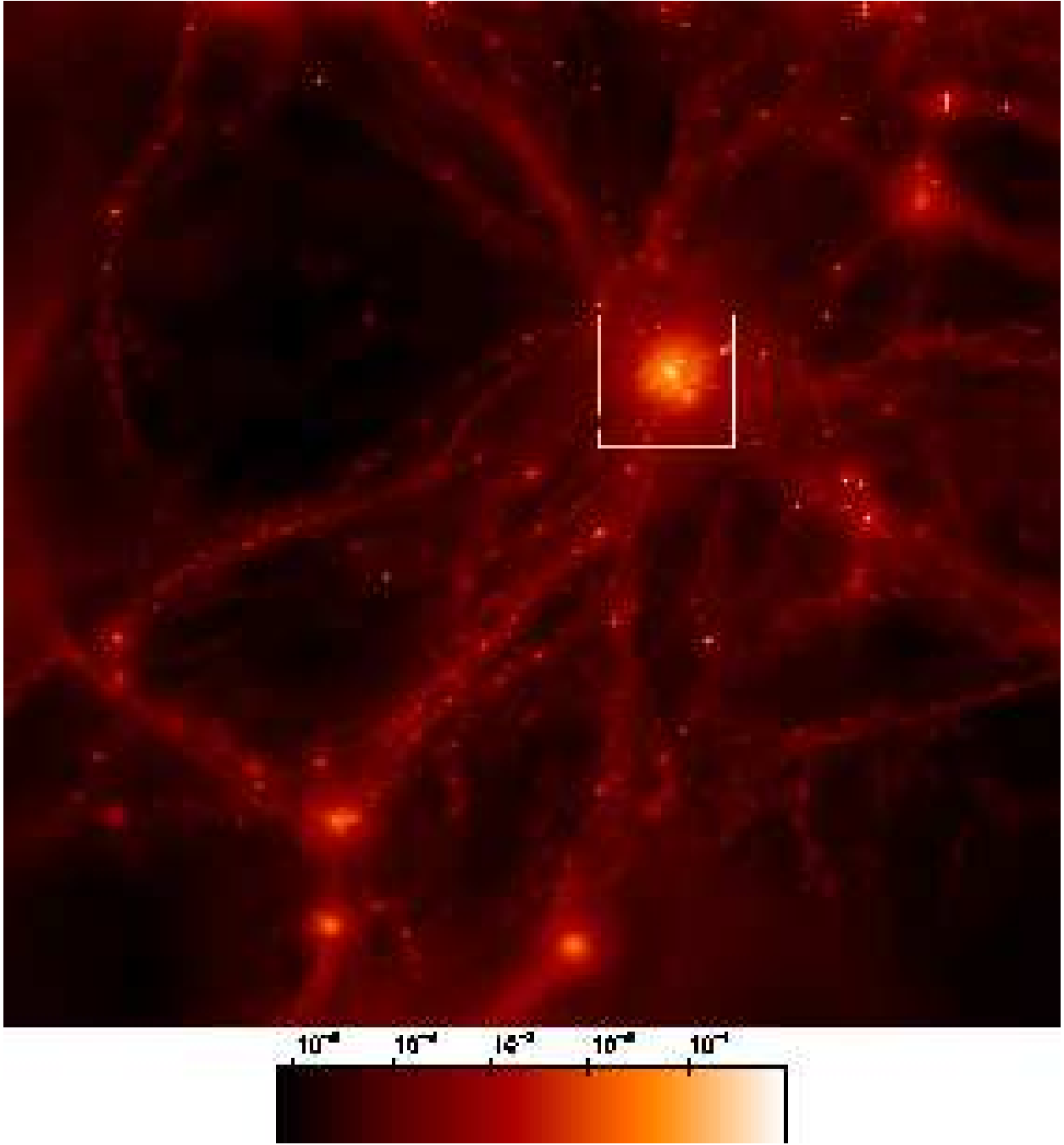


Fig. 1.— Projected gas density at the present day for the refined volume of C1. The highlighted square marks a $5 \text{ h}^{-1} \text{ Mpc}$ region around the dominant cluster. The entire image covers a region $37 \text{ h}^{-1} \text{ Mpc}$ by $36 \text{ h}^{-1} \text{ Mpc}$. The color bar at bottom indicates the relative range in surface density.

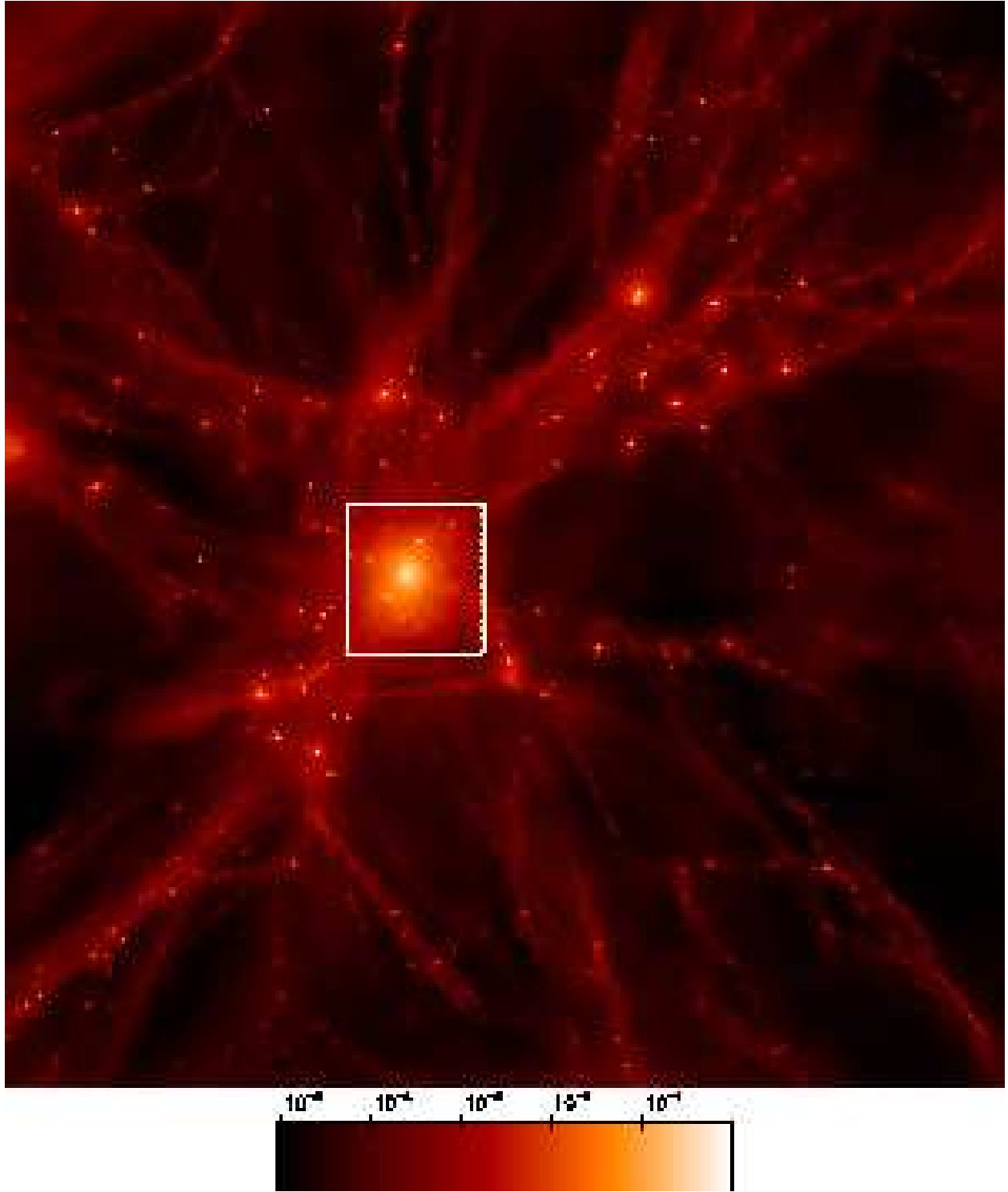


Fig. 2.— Projected gas density at present for the refined volume of C2. The highlighted square marks a $5 h^{-1}$ Mpc region around the dominant cluster. The entire image frames a region $35 h^{-1}$ Mpc by $38 h^{-1}$ Mpc. The color bar at bottom indicates the relative range in surface density.

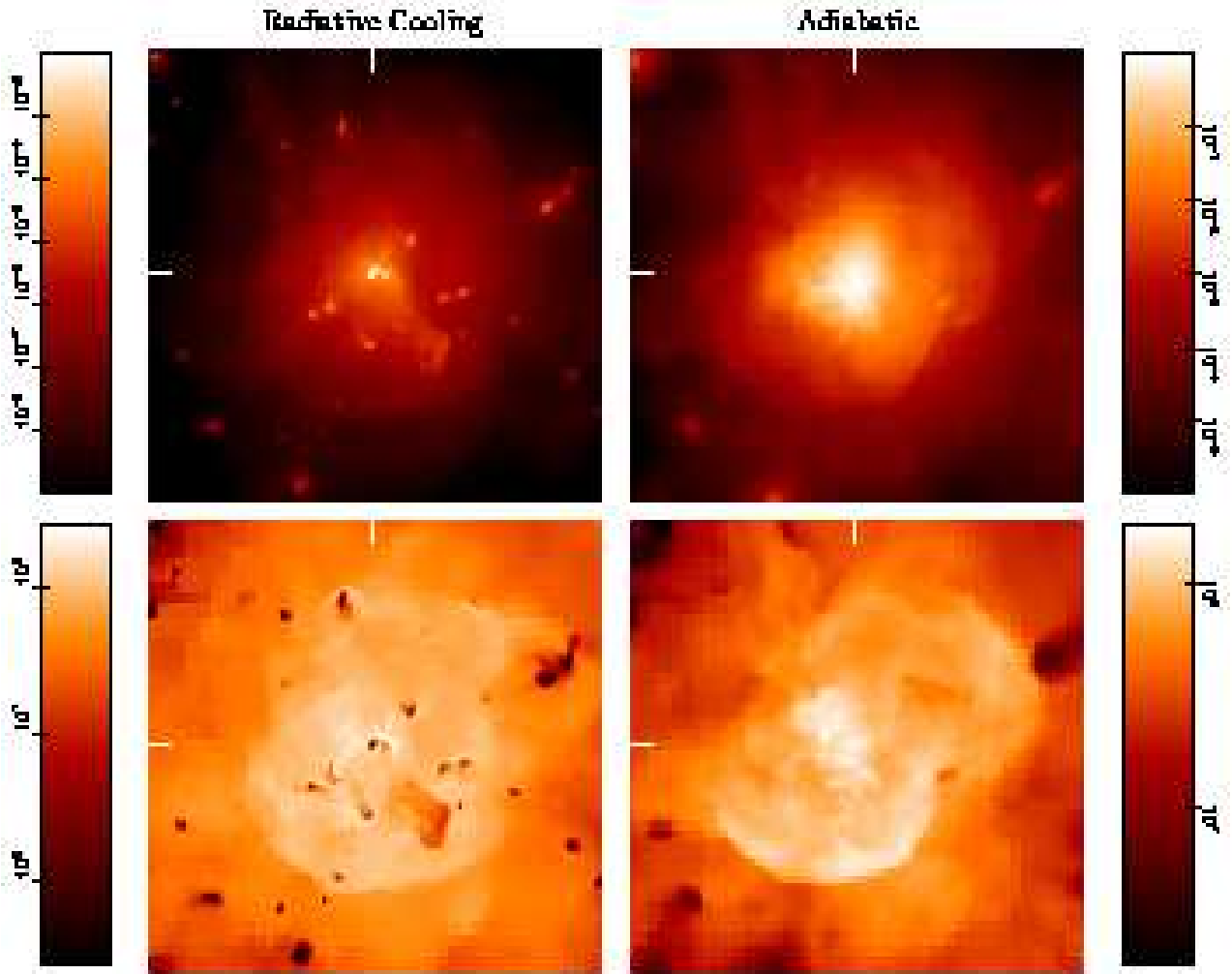


Fig. 3.— In the top row, we show the normalized, X-ray surface brightness image (in the 1 to 10 keV band) and at bottom the projected temperature map for radiative cooling and adiabatic realizations of C1 at a redshift of zero. The images show the central $5 h^{-1}$ Mpc region. The color bars indicate the range of surface brightness and emission-weighted temperature in Kelvin for each image. The tick marks above and to the left indicate the cluster center of mass.

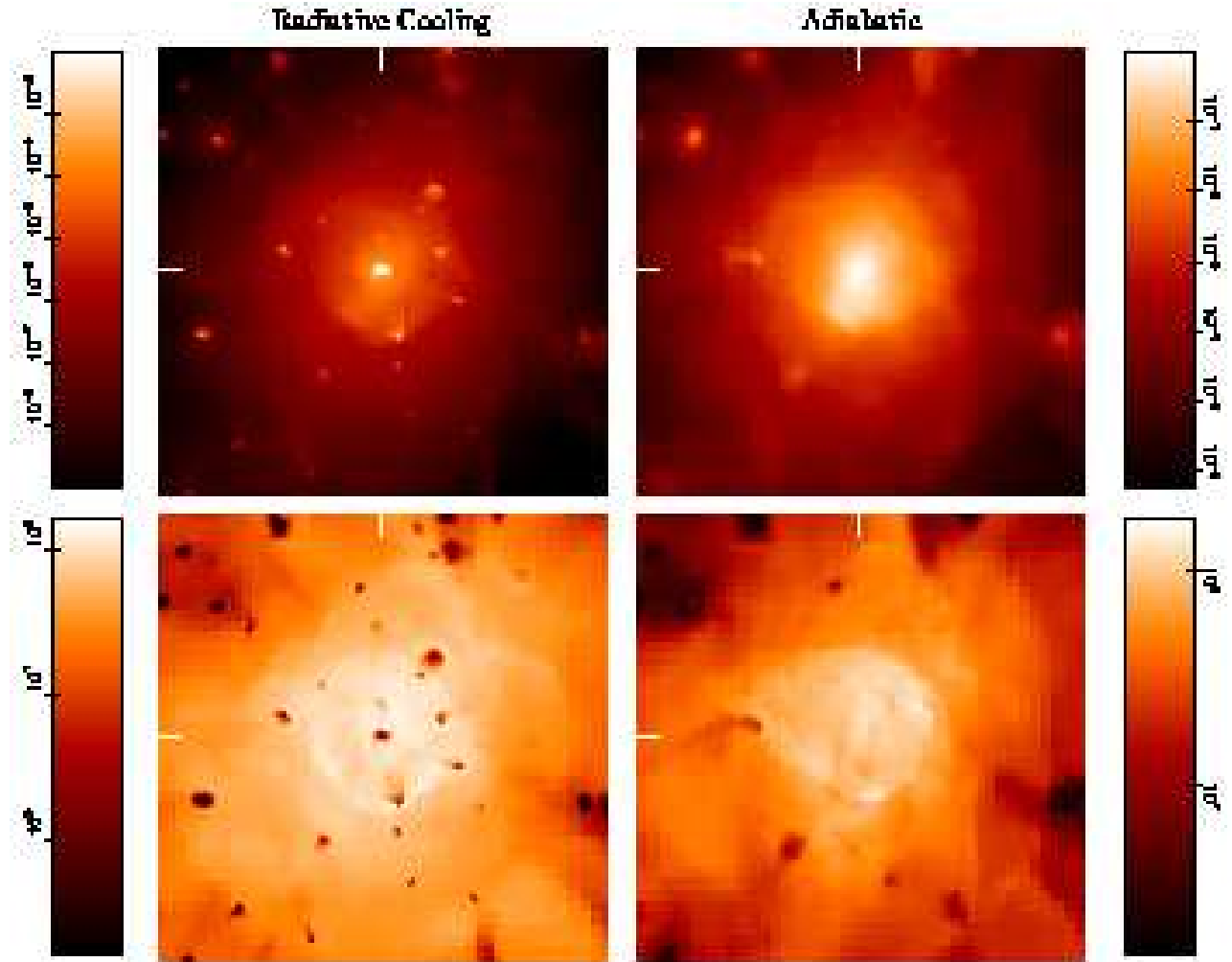
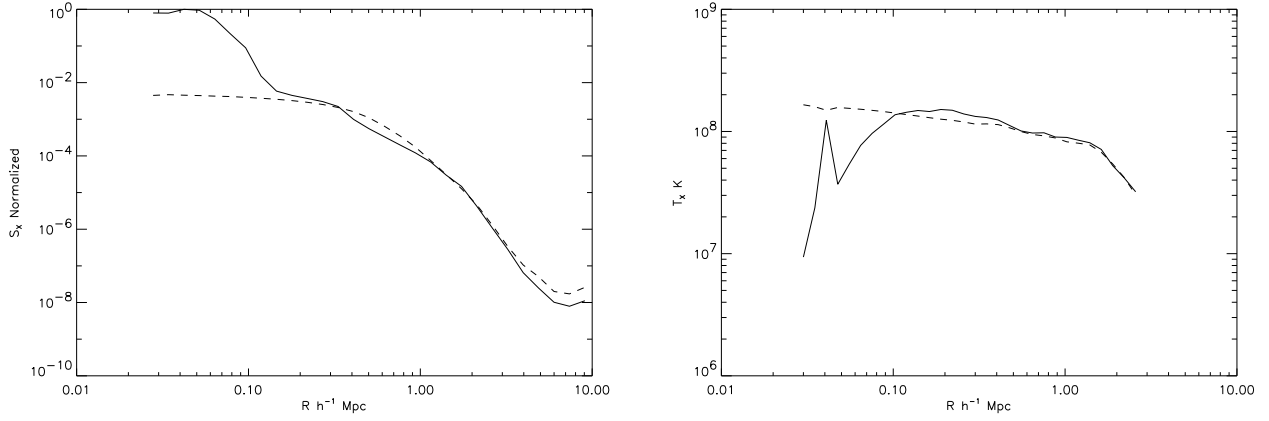


Fig. 4.— Projected, normalized X-ray surface brightness (top row) and projected temperature maps for C2 at a $z = 0.25$. The images show the central $5 h^{-1}$ Mpc. The center of mass of the central cluster is indicated by the tick marks. The color bars are as in Figure 3

Cluster 1



Cluster 2

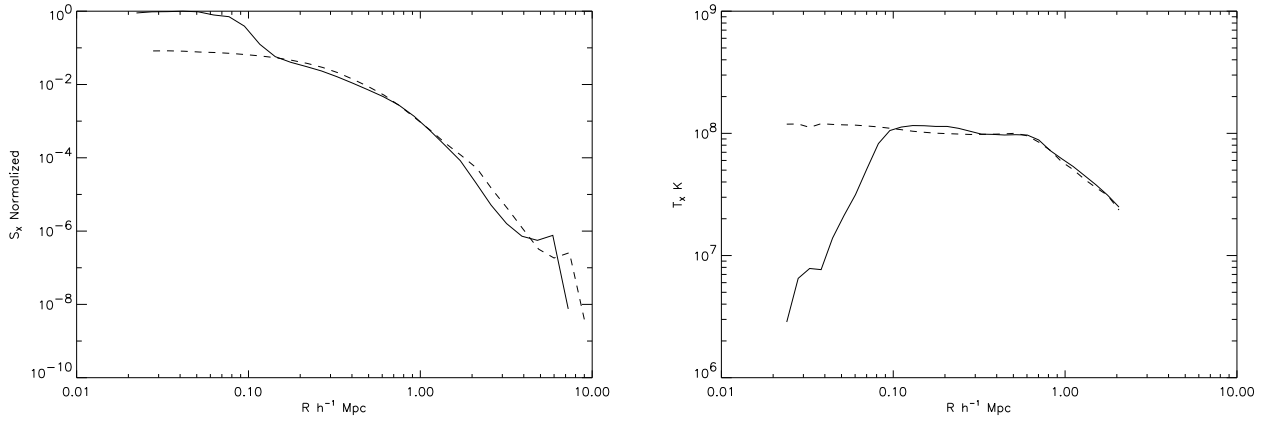


Fig. 5.— Profiles of the normalized X-ray surface brightness and projected luminosity-weighted temperature for C1 at $z = 0$ (top row) and C2 at $z = 0.25$ (bottom row). The solid curves correspond to the simulation with radiative cooling and the dashed curves are from the adiabatic simulation.

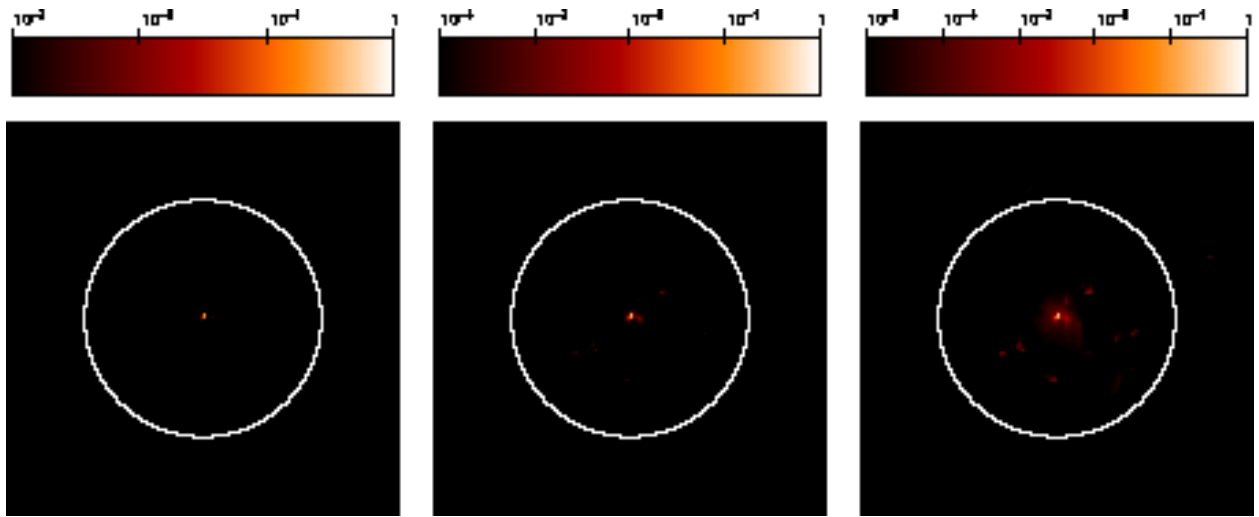


Fig. 6.— The normalized X-ray surface brightness for C1 at a redshift of zero for three image scales (from left to right, the minimum is 10^{-3} , 10^{-4} , and 10^{-5} of the peak intensity). A circle of radius $1.5 h^{-1} \text{ Mpc}$ and centered on the cluster center of mass is overlaid on the data. The X-ray emission is very strongly peaked at the cluster center, with a dynamic range of 10^4 only one subcluster is visible in the image and several other subclusters are visible if the dynamic range is extended to 10^5 .

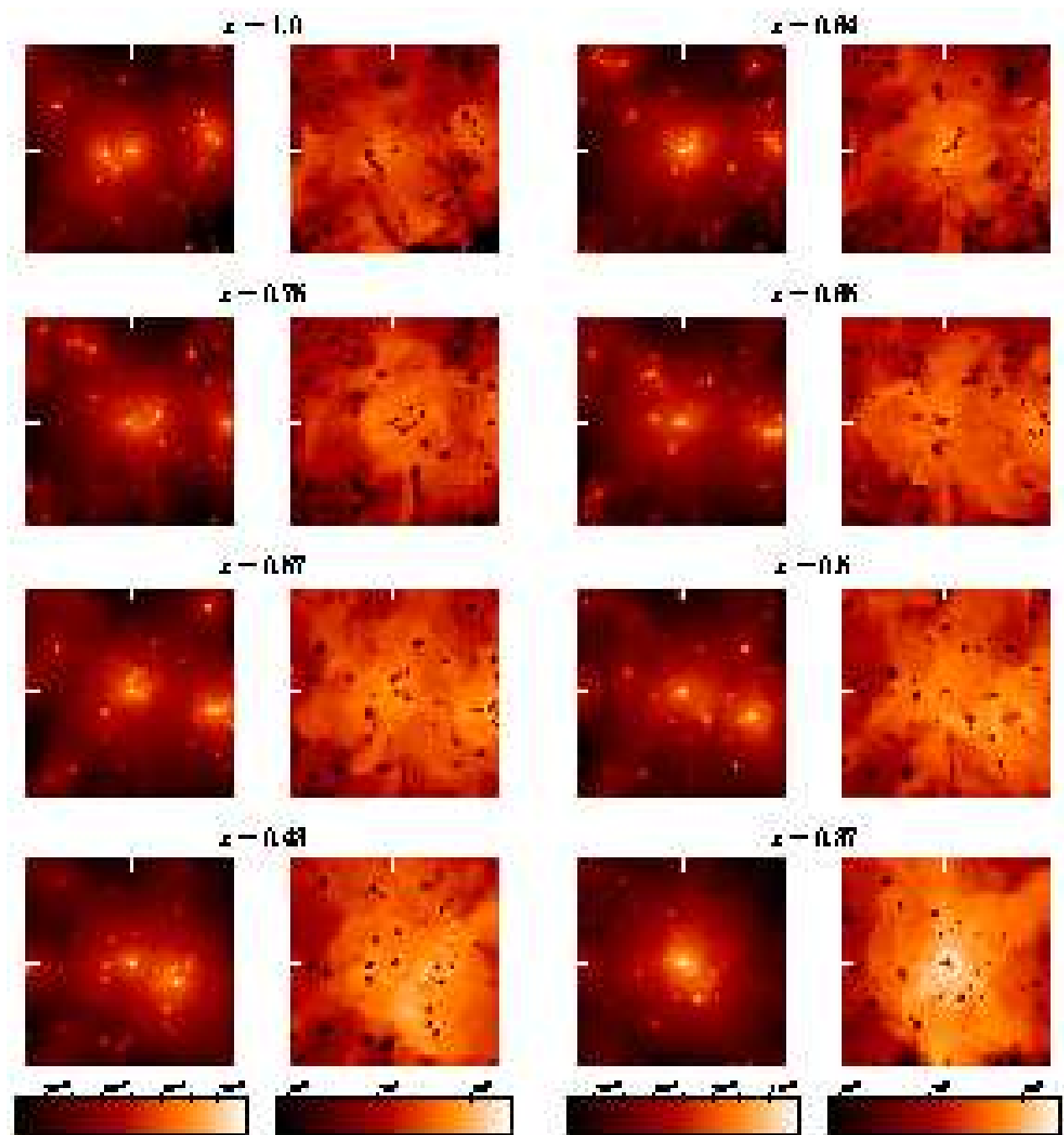


Fig. 7.— Projected, normalized X-ray surface brightness (left) and temperature maps (right) for C1 from a redshift of 1 to the present epoch in intervals of approximately 500 million years. The images are $5 h^{-1}$ Mpc on a side at the present epoch. All images were prepared on the same scale so that a given color corresponds to the same value throughout the table of images. The temperature is in Kelvin and the tick marks to the left and above each image mark the cluster center of mass.

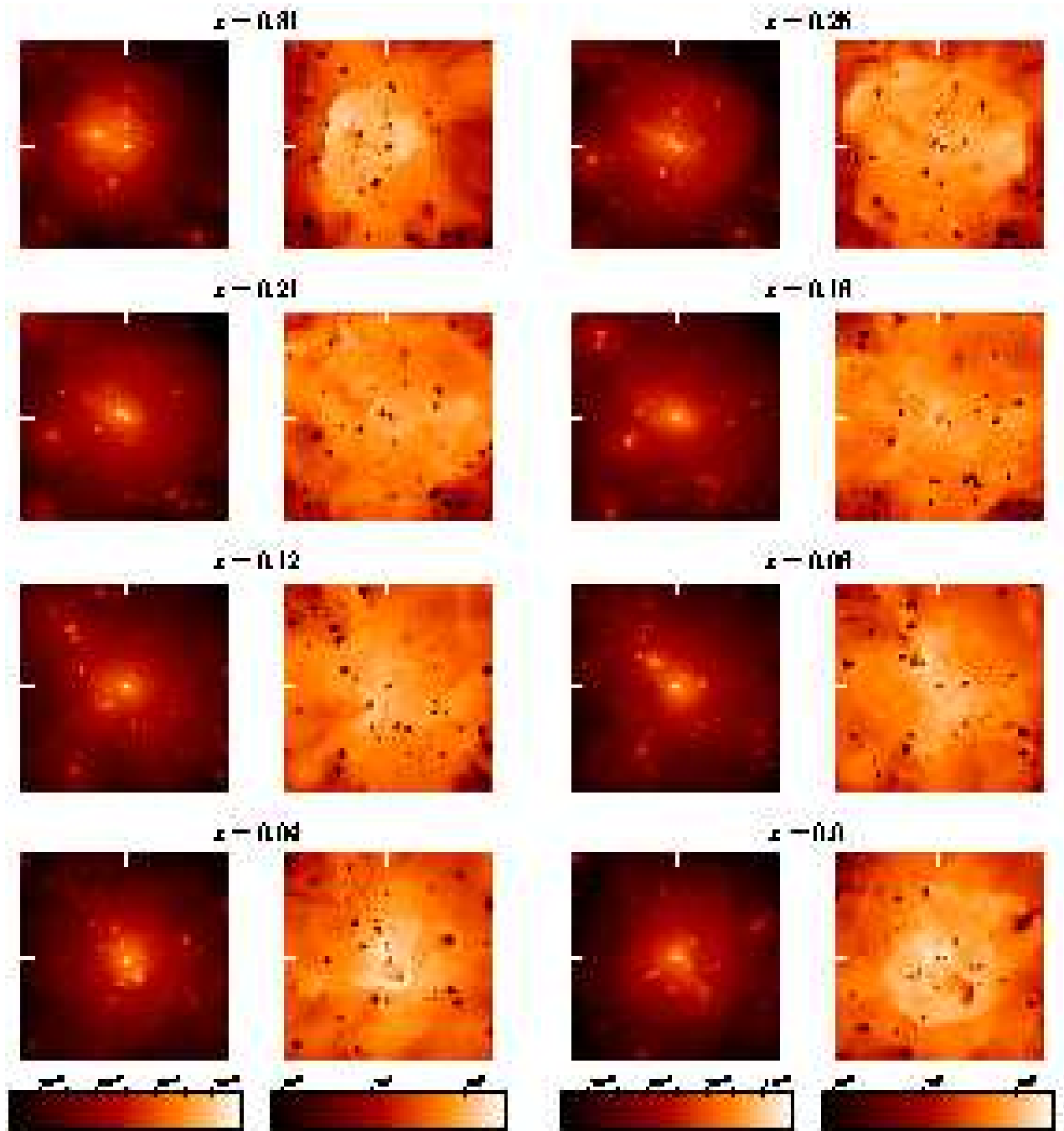


Fig. 7.— Projected, normalized X-ray surface brightness (left) and temperature maps (right) for C1 from a redshift of 1 to the present epoch in intervals of approximately 500 million years. As before the images are $5 h^{-1}$ Mpc on a side. All images were prepared on the same scale so that a given color corresponds to the same value throughout the table of images and the range of values are depicted in the color bars at bottom.

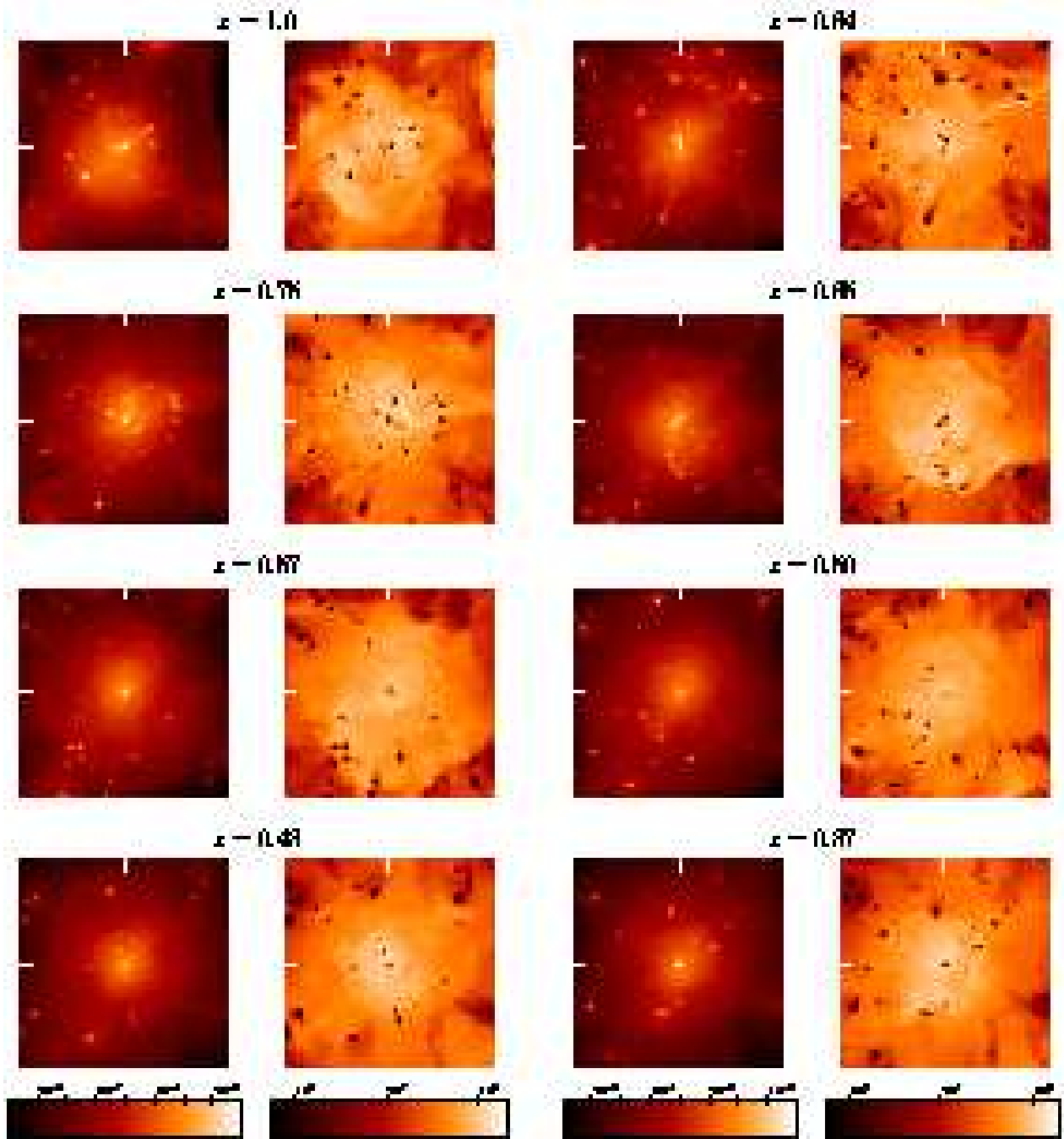


Fig. 8.— Projected, normalized X-ray surface brightness (left) and temperature maps (right) for C2 from a redshift of 1 to the present epoch in intervals of approximately 500 million years. As before the images are $5 h^{-1}$ Mpc on a side. All images were prepared on the same scale so that a given color corresponds to the same intensity or temperature level throughout the table of images.

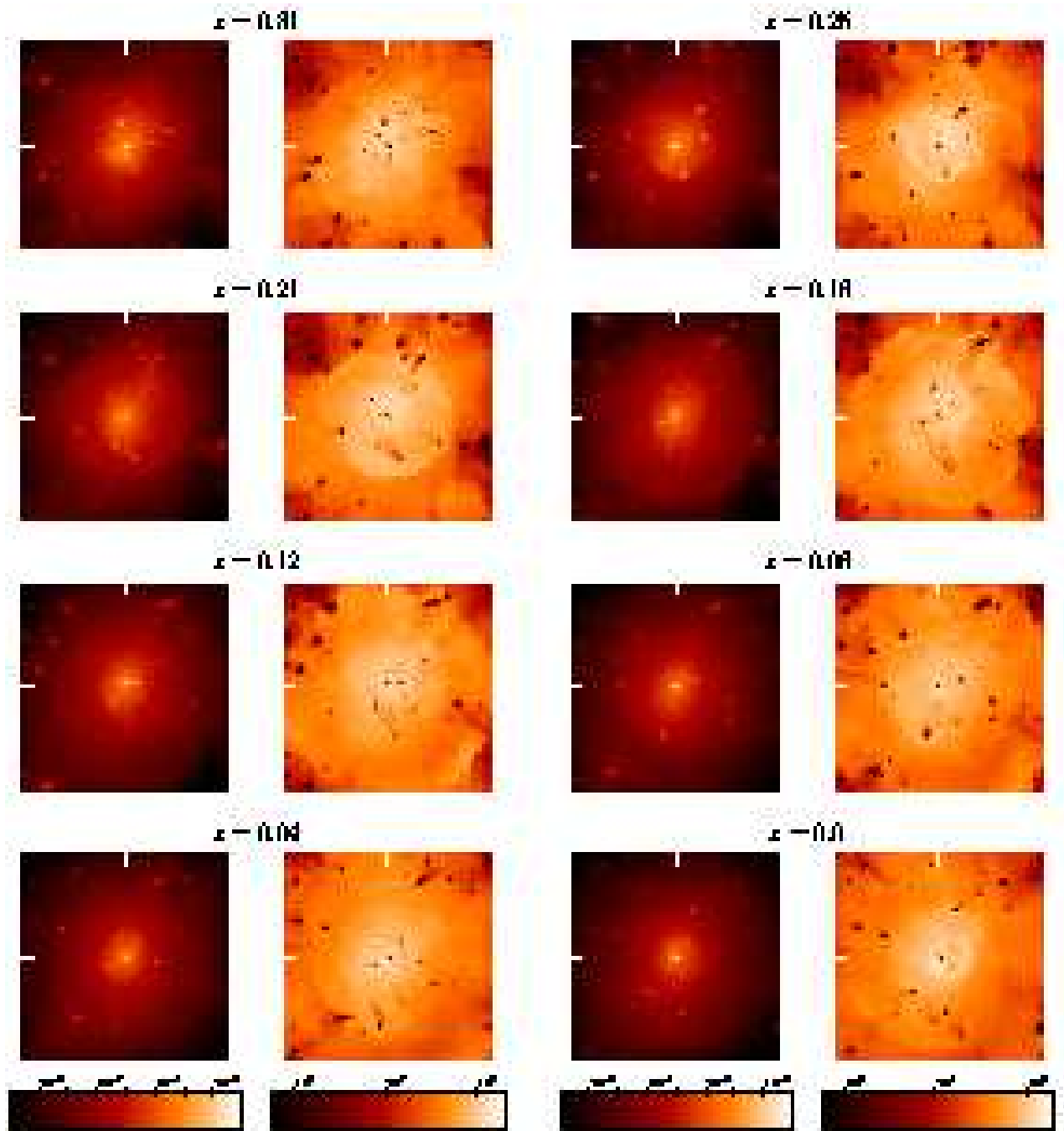


Fig. 8.— Projected, normalized X-ray surface brightness (left) and temperature maps (right) for Cluster 2 from a redshift of 1 to the present epoch in intervals of approximately 500 million years. As before the images are $5 h^{-1}$ Mpc on a side. All images were prepared on the same scale so that a given color corresponds to the same surface brightness or temperature level throughout the table of images.

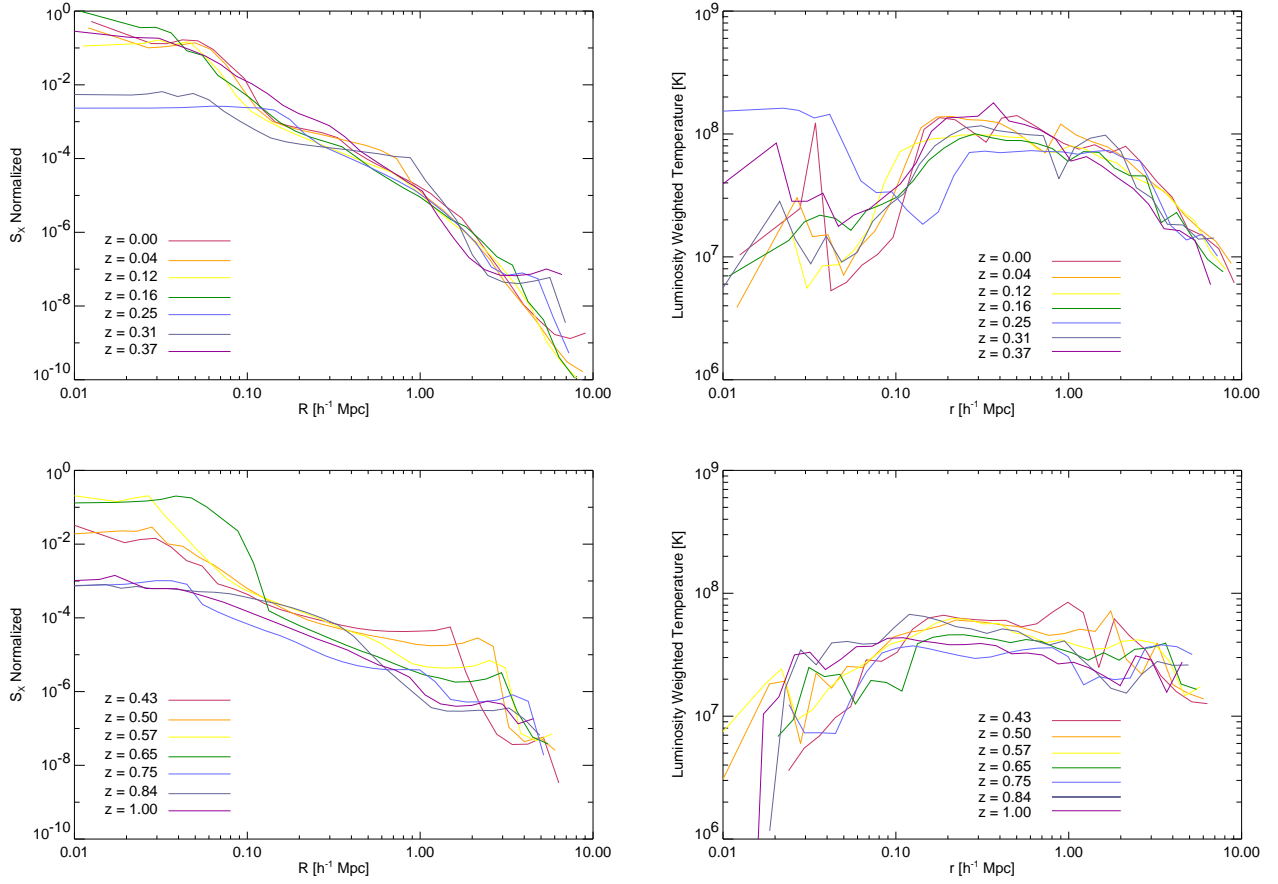


Fig. 9.— X-ray surface brightness profiles in the 1 to 10 keV band, normalized to the maximum value and spherically-averaged, luminosity-weighted temperature profiles for C1 at the indicated redshifts.

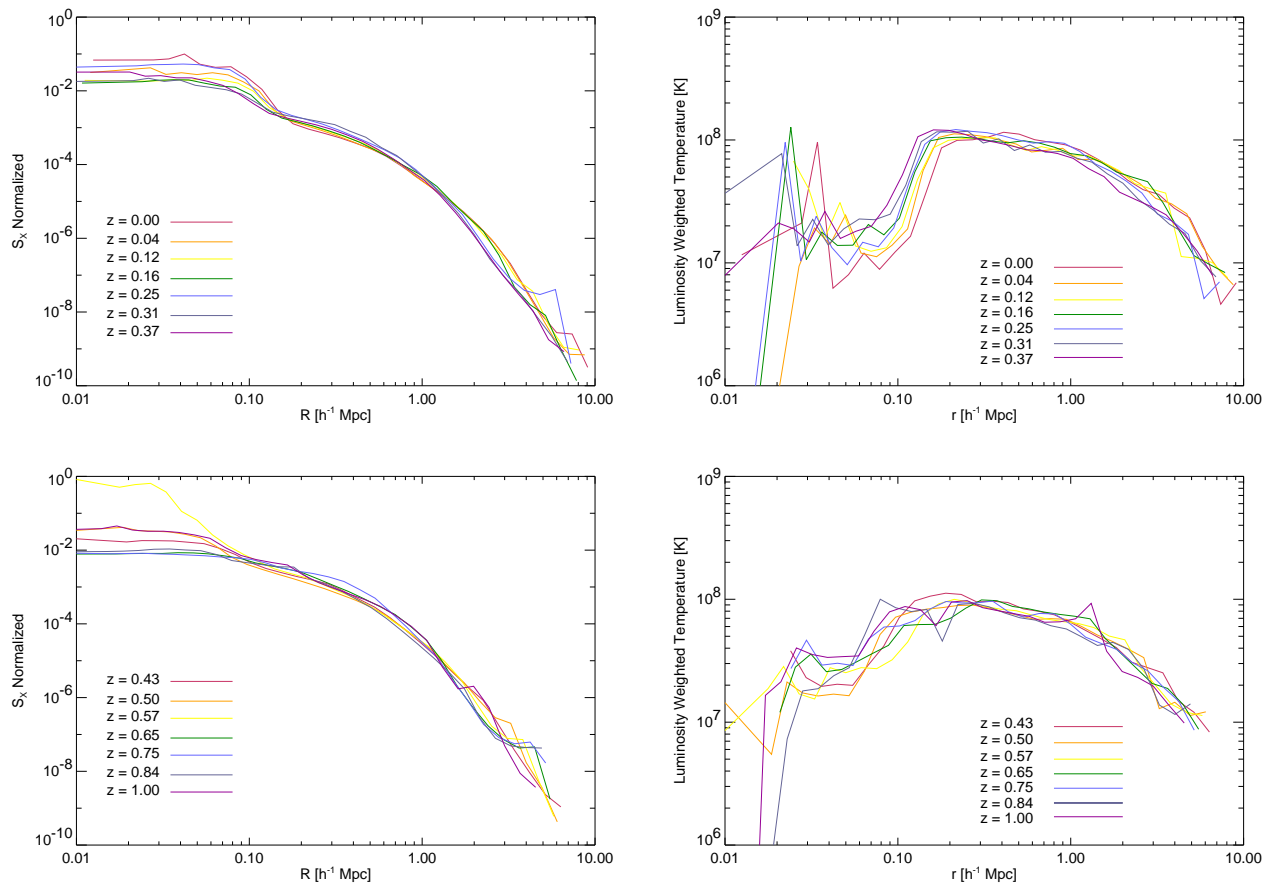


Fig. 10.— X-ray surface brightness profiles in the 1 to 10 keV band, normalized to the maximum value and spherically-averaged, emission-weighted temperature profiles for C2 at the indicated redshifts.

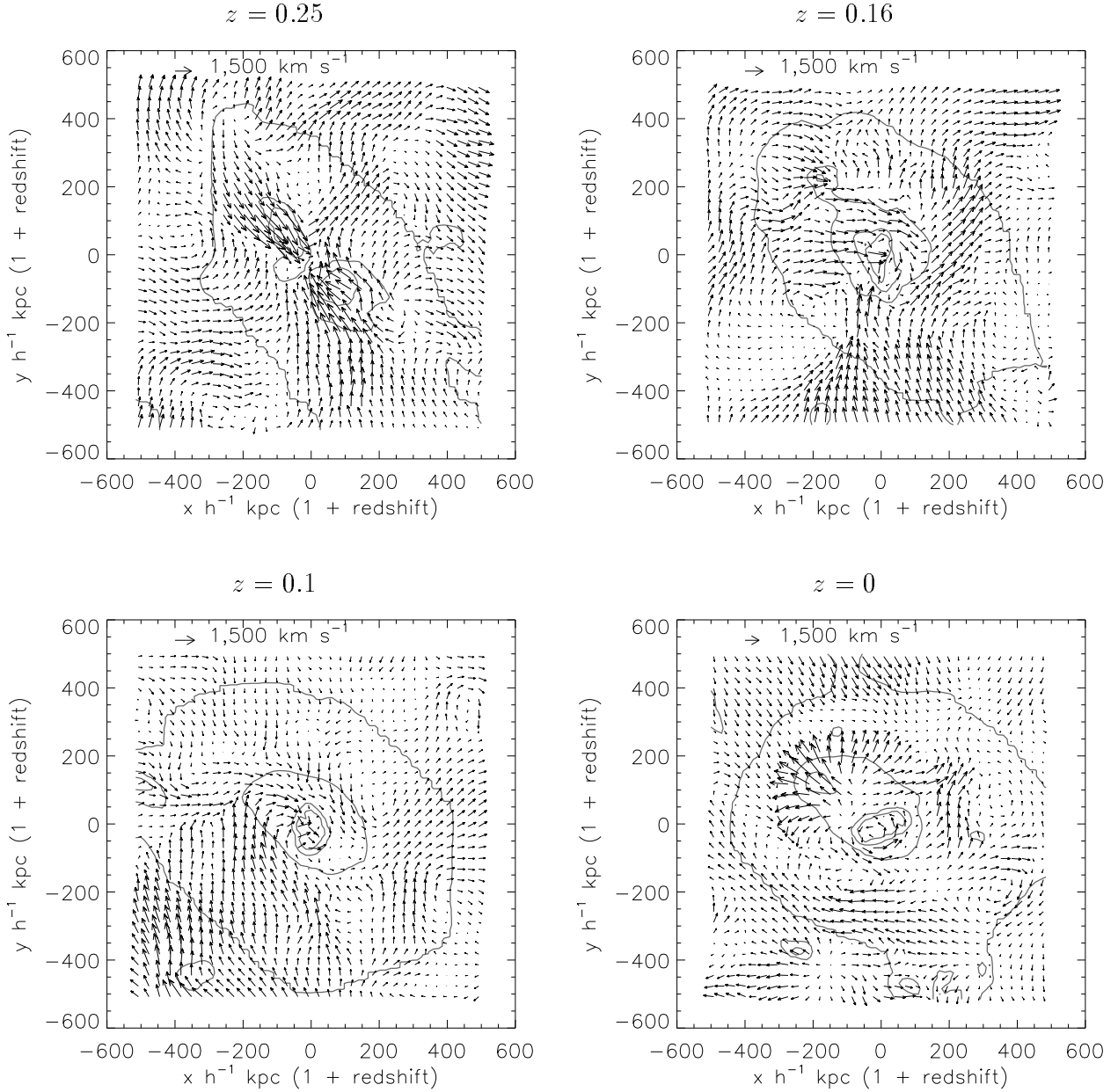


Fig. 11.— Velocity fields in the x-y plane for cluster C1 at the indicated epochs. The scale of the velocity vectors is indicated by the vector with magnitude $1,500 \text{ km s}^{-1}$ at the top of each plot. Projected X-ray surface brightness contours are also shown to help outline the flow field. The four contours are spaced logarithmically from 1×10^{-2} to 1×10^{-5} of the peak value.

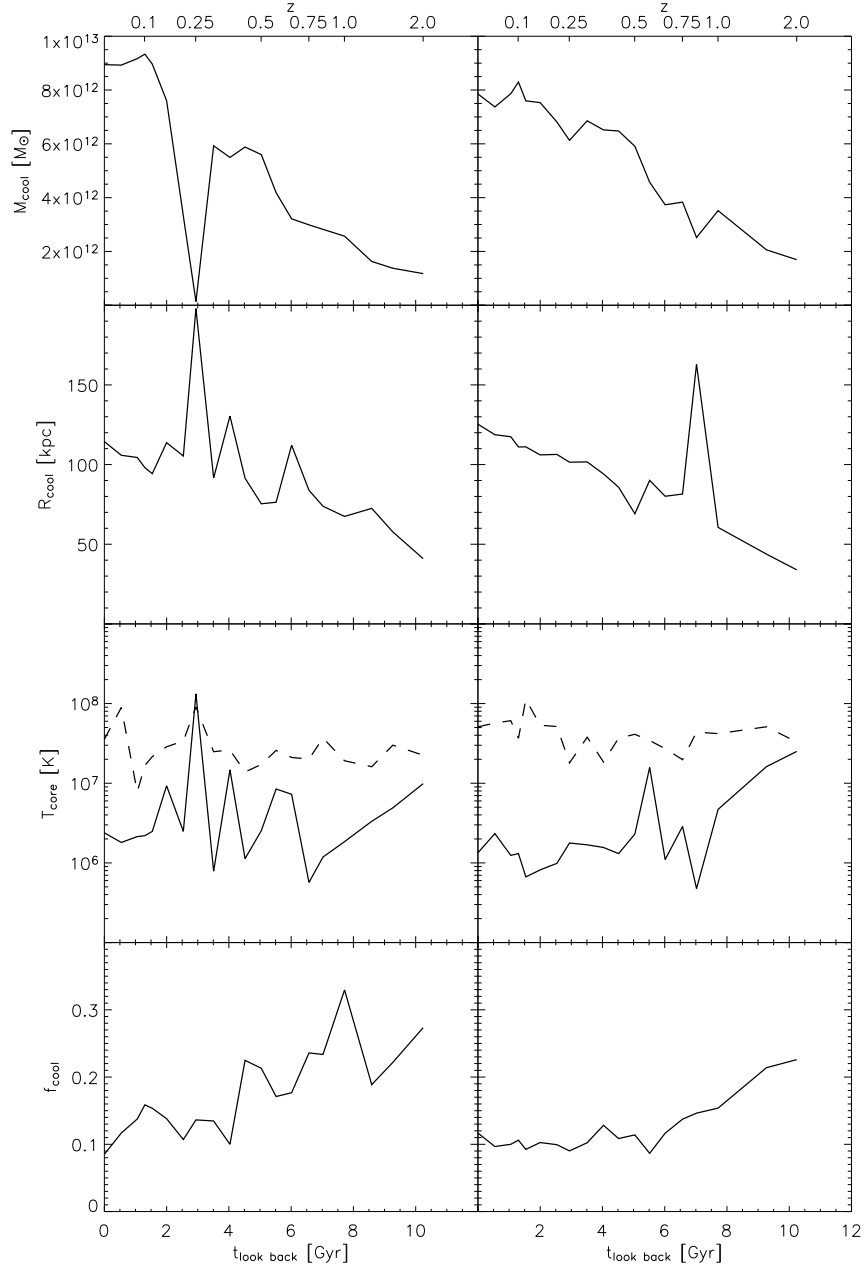


Fig. 12.— Mass of cold gas within $100 h^{-1}$ kpc of the cluster center (top row), the cooling radius (second row), central core temperature (third row), and fraction of cool gas (bottom row) all as a function of lookback time for the simulated clusters C1 (left) and C2 (right). The core temperature is measured in two ways; the solid curves correspond to the physical gas temperature averaged over a sphere of radius $50 h^{-1}$ kpc centered on the cluster center of mass while the dashed curves correspond to the average within a $50 h^{-1}$ kpc circle of the projected, emission-weighted temperature field. The redshifts for a given lookback time are shown at top for reference.

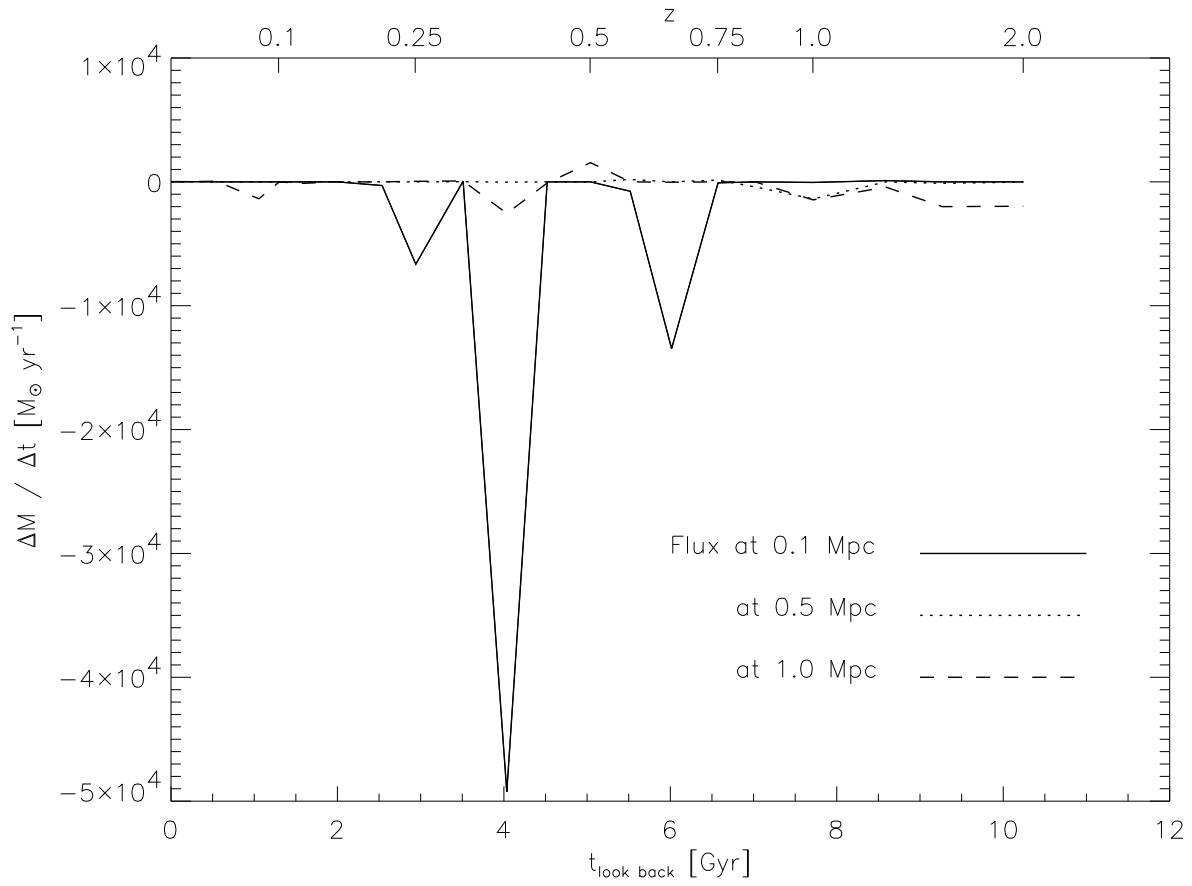


Fig. 13.— Flux of cool gas (in M_{\odot}/yr) through spheres of radius 0.1, 0.5, and 1.0 Mpc centered on the cluster center of mass throughout the C1 simulation.

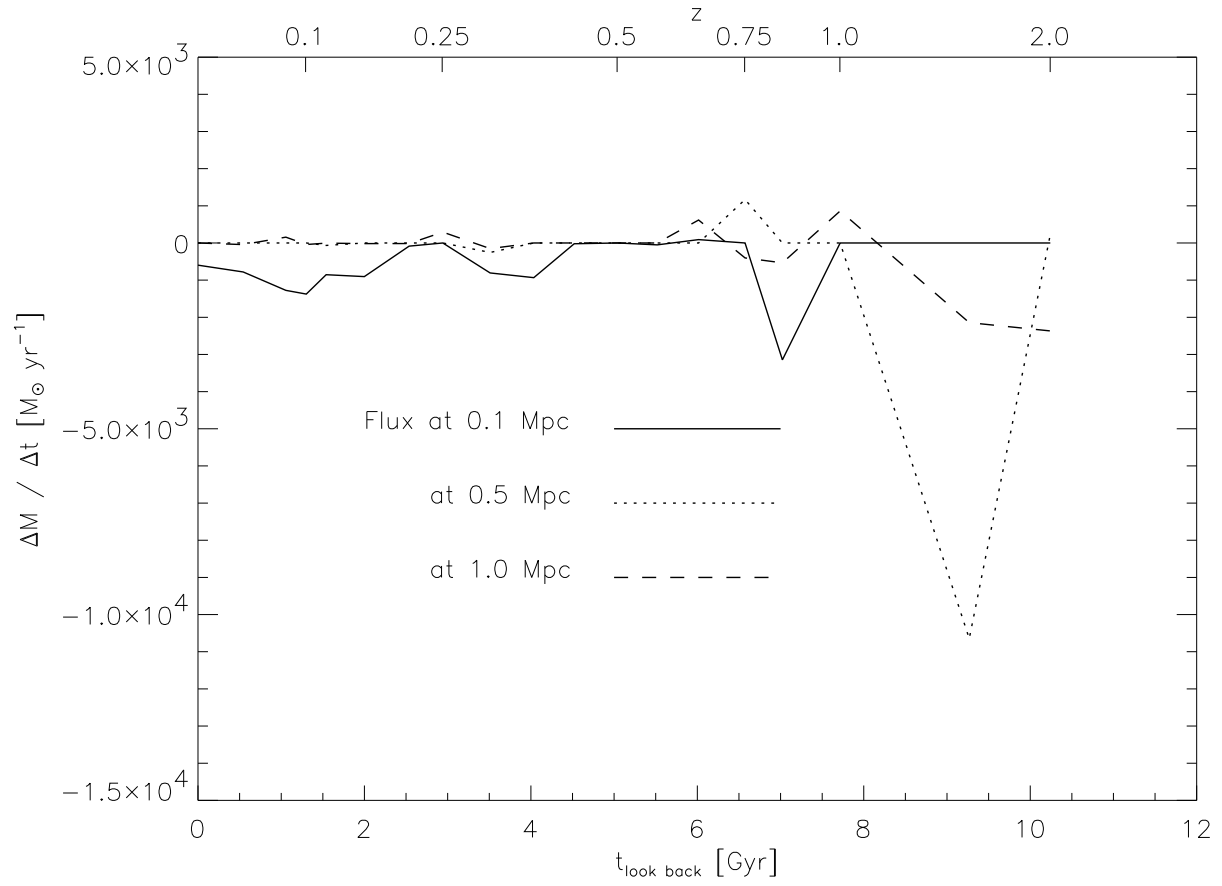


Fig. 14.— Flux of cool gas (in M_\odot/yr) through spheres of radius 0.1, 0.5, and 1.0 Mpc centered on the cluster center of mass for the C2 simulation.

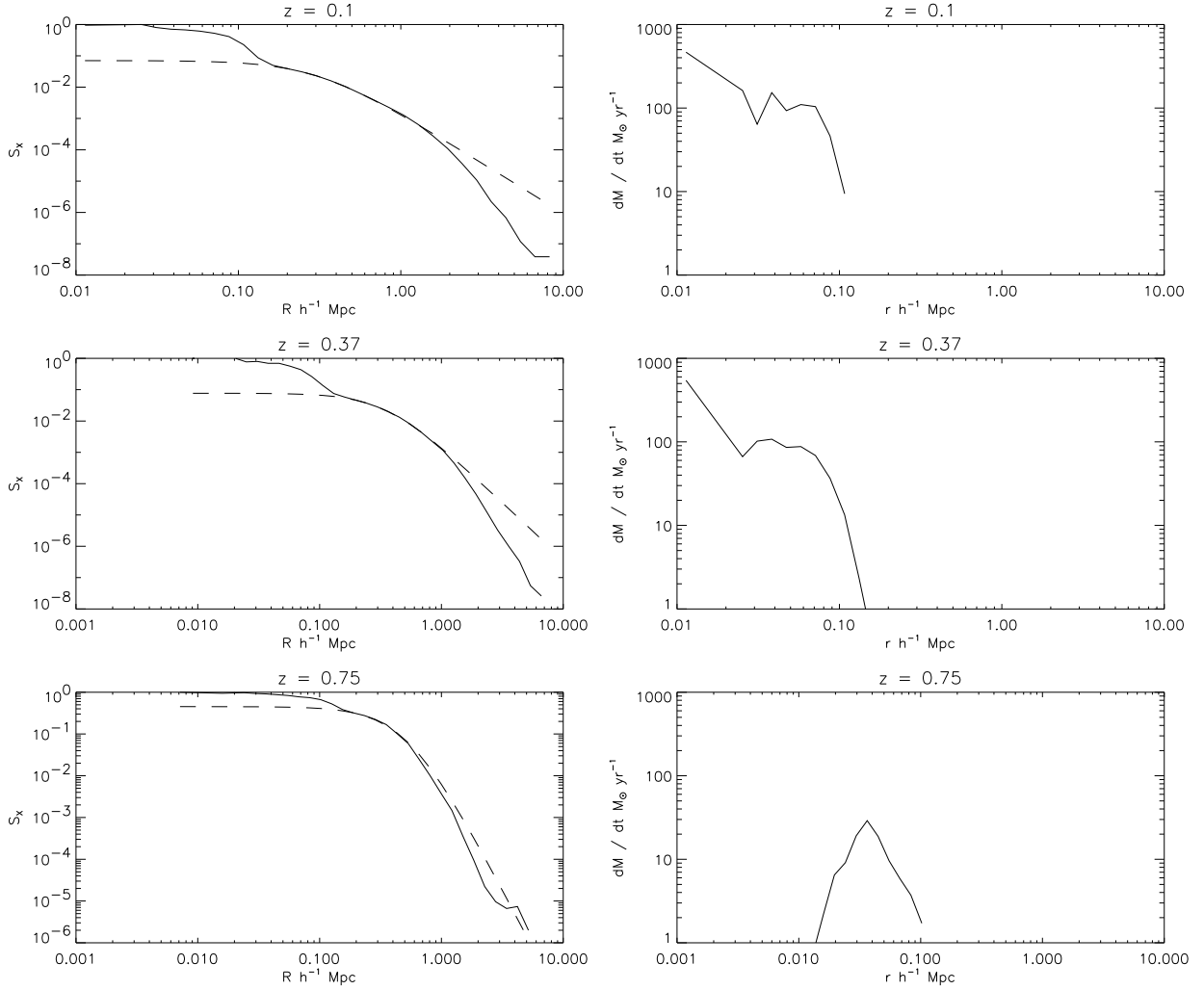


Fig. 15.— In the left column the predicted surface brightness profile (solid curve) and the fit isothermal profile (dashed line) for cluster C2 at the indicated redshift. The right column shows the implied cooling flow rate given the temperature profile. At a redshift of $z = 0.75$ the cluster is in the final stages of a major merger and the presence of two luminosity maxima on opposite sides of the cluster center of mass gives rise to the decline in the inferred cooling rate.

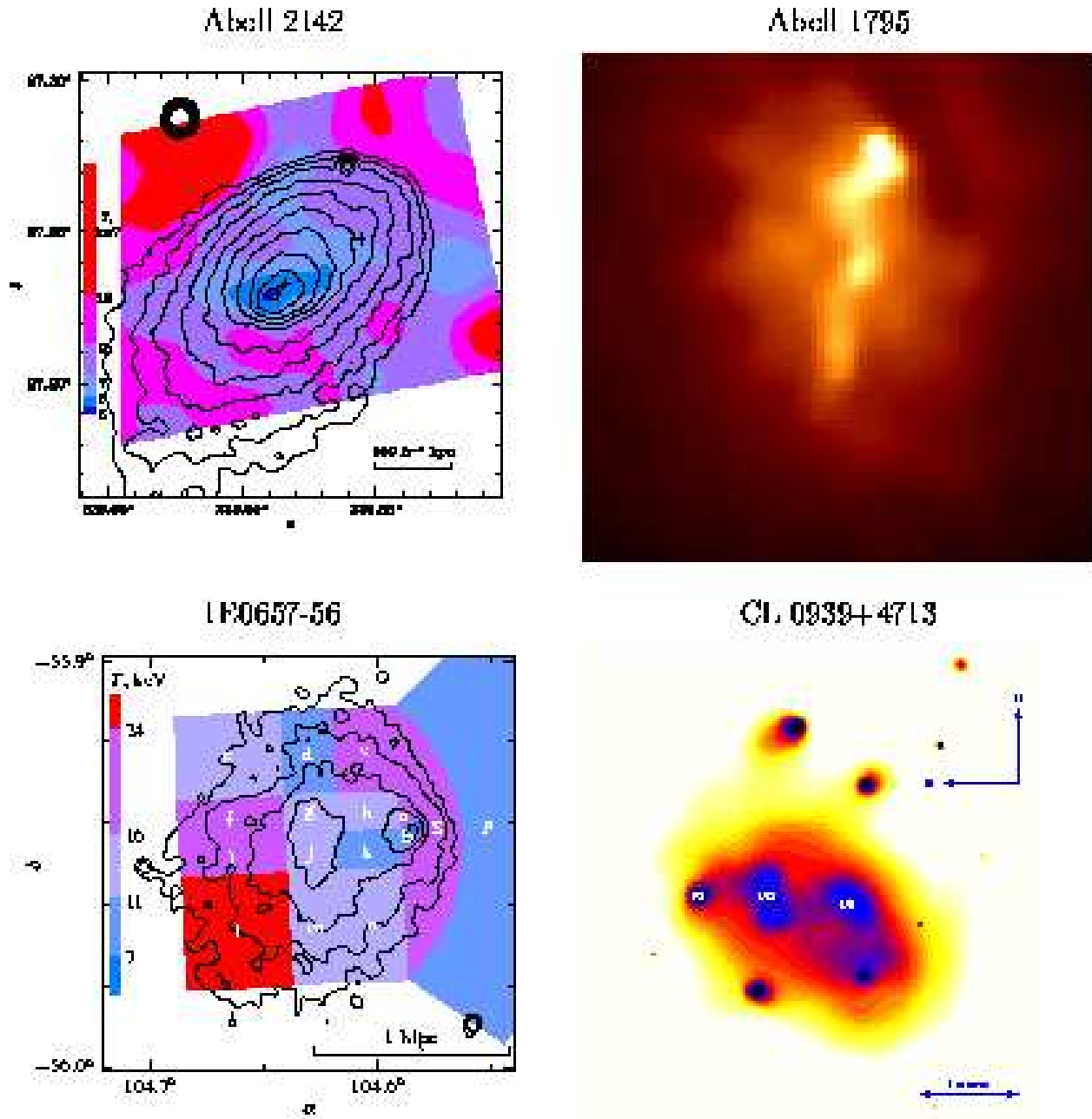


Fig. 16.— Recent results from *Chandra* and *XMM* emphasizing the rich and complex nature of cool core clusters. Clockwise from upper left: Abell 2142 with its irregular temperature distribution and “cool fronts” (Markevitch *et al.* 2000), the filamentary distribution of cool material in the core of Abell 1795 (Fabian *et al.* 2001), the colliding “bullet subcluster” system 1E0657-56 (Markevitch *et al.* 2002), and finally a more distant cluster with significant central substructure, CL 0939+4713 (De Filippis *et al.* 2001).